Kröger, Jörg; Néel, Nicolas; Wehling, Tim O.; Brandbyge, Mads:

Local probes of graphene lattice dynamics

Original published in:	Small methods. - Weinheim : WILEY-VCH Verlag GmbH & Co. KGaA. - 4 (2020), 5, art. 1900817, 18 pp.
Original published:	2020-03-08
ISSN:	2366-9608
DOI:	10.1002/smtd.201900817
[*Visited:*	2020-05-18]

small method
www.small-methods.com

Local Probes of Graphene Lattice Dynamics

Jörg Kröger, Nicolas Néel, Tim Oliver Wehling, and Mads Brandbyge*

Inelastic electron tunneling spectroscopy with a scanning tunneling microscope is a powerful method to excite and detect vibrational quanta with atomic resolution. The focus of this review article is on the local spectroscopy of graphene phonons. The experimental observation of their spectroscopic signatures together with theoretical modeling highlight the importance of the graphene–surface as well as the graphene–tip hybridization, the electron–phonon coupling strength, phonon-mediated tunneling, local doping profiles, and the phonon density of state for the measured signal. Meanwhile, a comprehensive understanding of the underlying mechanisms has been attained and justifies an overview on available findings.

1. Introduction

Graphene is the two-dimensional (2D) honeycomb lattice of sp^2-bonded C atoms and exhibits outstanding properties, such as high charge carrier mobility and ballistic electron transport at room temperature.[1–4] Phonons of the C lattice may affect charge transport in graphene, as reported for the reduction of ballistic electron transport due to electron scattering from optical phonons.[5–7] Moreover, the relation between phonons and thermal transport in graphene becomes increasingly important.[8] Therefore, it is not surprising that graphene phonons and their dispersion have attracted substantial interest. Laterally averaging spectroscopy methods,[9–16] for instance, enabled the extraction of the electron–phonon coupling strength,[17] the possible distortion of the Dirac cone,[18] and the graphene–substrate hybridization.[19] As an example, **Figure 1** shows measured and calculated phonon dispersion branches of graphene on Ir(111).[13] All phonon dispersion branches (left panel of Figure 1) were measured throughout the graphene Brillouin zone (BZ) (right panel) using angle-resolved electron energy loss spectroscopy with an Ibach spectrometer.[20] The individual branches for the out-of-plane acoustic (ZA), transverse acoustic (TA), longitudinal acoustic (LA), out-of-plane optical (ZO), transverse optical (TO), and longitudinal optical (LO) phonon modes are in good agreement with calculations (dashed lines). The dispersion curves are very similar to the dispersion relations of pristine graphene[21,22] and graphite.[21–24] Deviations mainly concern the Kohn anomaly of the highest optical phonon branches at **K** and the nonzero energy of the ZA phonon at **Γ**, both of which were previously discussed.[13]

The local probing of graphene phonons by inelastic electron tunneling spectroscopy (IETS) with a scanning tunneling microscope (STM) is particularly appealing since the impact of, e. g., atomic defects, molecular adsorbates, and doping profiles, on the lattice dynamics can be explored with ultimate spatial resolution. So far, STM-IETS of graphene phonons has been reported from graphene on SiC,[25–29] SiO_2,[30,31] graphite,[32] and SiO_2 covered with hexagonal boron nitride (h-BN)[33,34] as well as single-crystalline $SrTiO_3$ surfaces.[35] For graphene on metal surfaces several works are likewise available. Delaminated graphene nanostructures on Pt(111)[36] and Ir(111),[37] graphene on Rh, Pd, and Cu foils,[35] and graphene-covered Ir(111) intercalated by alkali metals[38] showed phonon signatures in IET spectra.

The observation of graphene phonon signatures in IETS imposes challenges on our current understanding of the IET process. In a seminal work,[30] the observation of **K**-point graphene phonons in spectroscopy of the differential conductance (dI/dV; I: current; V: bias voltage) of graphene-covered SiO_2 was reported with an exceptionally high spectroscopic signal strength. The phonon excitation was accompanied by an order-of-magnitude increase of dI/dV at the threshold bias voltage needed to excite the phonon. To explain this remarkable observation, the phonon-mediated tunneling mechanism was conceived that relies on the virtual preservation of the free-graphene electronic structure after adsorption on SiO_2, notably of an electronic gap at the **Γ**-point of the BZ and the Dirac point close to the Fermi energy (E_F) at **K** (vide infra). Phonon-assisted electron tunneling was likewise suggested as a rationale for conductance peaks in multilayer graphene–h-BN–graphene transistors.[39] This work[39] shows that for stacked van der Waals heterostructures phonon-mediated tunneling represents an efficient mechanism for carrying the current perpendicular

Prof. J. Kröger, Dr. N. Néel
Institut für Physik
Technische Universität Ilmenau
D-98693 Ilmenau, Germany
E-mail: joerg.kroeger@tu-ilmenau.de
Prof. T. O. Wehling
Bremen Center for Computational Materials Science
University Bremen
D-28359 Bremen, Germany
Prof. T. O. Wehling
Institute for Theoretical Physics
University Bremen
D-28359 Bremen, Germany
Prof. M. Brandbyge
Center for Nanostructured Graphene
Department of Physics
Technical University of Denmark
DK-2800 Kongens Lyngby, Denmark
The ORCID identification number(s) for the author(s) of this article can be found under https://doi.org/10.1002/smtd.201900817.

DOI: 10.1002/smtd.201900817

to the layers, which otherwise would be suppressed due to the momentum mismatch induced by the misalignment of the crystalline lattices.

The emerging picture for observing an enhanced graphene phonon signal in IETS, therefore, requires the nearly genuine graphene electronic structure that promotes phonon emission wave vectors corresponding to the **K**-point. Several findings, however, have questioned this picture. For exfoliated graphene on SiO_2, phonon spectroscopic signatures were not observed, albeit the quasi-free behavior of graphene.[40,41] In addition, graphene phonons throughout the BZ[34] or at the **M**-points of the BZ[37,38] were mapped in dI/dV spectroscopy. Moreover, alkali metal-intercalated graphene[38] as well as graphene on Ru(0001),[42,43] which supposedly exhibit a stronger hybridization with the substrate, likewise exhibit clear phonon signatures in IETS. These results call for an extension or even alteration of the emerging picture and insistently demonstrate that IETS of graphene phonons is a vividly debated topic.

The key target of this review article is a contribution to the understanding of IETS data of graphene phonons that have been available to date. The article is organized as follows. After the introduction into the field (Section 1), graphene preparation methods for metal surfaces are briefly reviewed and the IETS technique is explained in Section 2. Section 3 presents experimental results obtained from graphene on semiconducting surfaces (Section 3.1), semimetals (Section 3.2), and metals (Section 3.3). Theoretical modeling is presented in Section 3.4. Summarizing and concluding remarks are given in Section 4.

2. Experimental Section

2.1. Preparation of Graphene on Metal Surfaces

Originally, graphene was prepared as a free-standing 2D layer of C via exfoliation from graphite.[1] In its adsorbed form, however, it has been known even longer. The formation of graphene was first observed on Pt and Ru single-crystalline surfaces.[44–48] In these early surface physics experiments, the annealing of the metal samples led to the segregation of C impurities to the surface where the characteristic honeycomb lattice of graphene was formed subsequently. The C impurities needed for the segregation process are either genuine to the nominally clean metal sample or result from intentional doping at elevated temperature.[49–52] Apart from segregation, reactions involving hydrocarbon molecules on metal surfaces unveiled graphitic layers that contained a few layers or even a single layer of graphene.[53] Thermal decomposition of C-containing molecules and subsequent forming of graphene was successfully demonstrated with acetylene (C_2H_2), methane (CH_4), ethylene (C_2H_4), propene (C_3H_6), benzene (C_6H_6), toluene (C_7H_8), cyclohexane (C_6H_{12}), *n*-heptane (C_7H_{16}), and CO on catalytically active metal surfaces, such as Ir(111).[54–57] The appealing advantage of graphene growth via thermal decomposition of hydrocarbon molecules is the control of the resulting C film thickness to a single layer. Combining segregation of C impurities and thermal decomposition of hydrocarbon molecules has enabled the preparation of graphene stackings with a controlled number of layers.[58]

Jörg Kröger studied physics at the RWTH Aachen University. He received his Ph.D. degree in 1995 for a work on surface phonons with electron energy loss spectroscopy. Postdoctoral studies with angle-resolved photoelectron spectroscopy were performed at the University of Zurich and the synchrotrone ELETTRA. At the Christian-Albrechts University of Kiel, he was in charge of building and operating a custom-made scanning tunneling microscope. Since March 2010, he has been a professor at the Technical University of Ilmenau, where he uses low-temperature scanning probe techniques to study the quantum physics of surfaces and interfaces.

Nicolas Néel is a senior scientist at the Technical University of Ilmenau. His main research activities deal with the investigation of atomic scale structures and 2D layers on surfaces using scanning tunneling and atomic force microscopy. He studied at the Université Paris Sud XI (France), where he obtained his DEA in physics in 1999. He did his Ph.D. at the Commissariat à l'Energie Atomique in Saclay (France), where he investigated the growth of metallic nanostructures and was graduated in physics in 2004. From 2004 to 2011, he worked at the Christian-Albrechts University of Kiel as a postdoctoral fellow in the field of atomic/molecular contacts and magnetic systems.

Mads Brandbyge is a professor at the Technical University of Denmark (DTU), Dept. of Physics, and the Center of Excellence for Nanostructured Graphene (CNG). He obtained his Ph.D. degree in physics from DTU in 1997, and after postdoctoral positions at the University of Tokyo and the Microelectronics Centre (MIC) at DTU, he was promoted to the positions of Associate Professor in 2004 and Full Professor in 2015 at DTU. His research interests are focused on theory of transport properties of nanostructures with focus on electron and heat transport, electron–phonon interaction, and current-induced effects. His group has developed widely used methods and software.

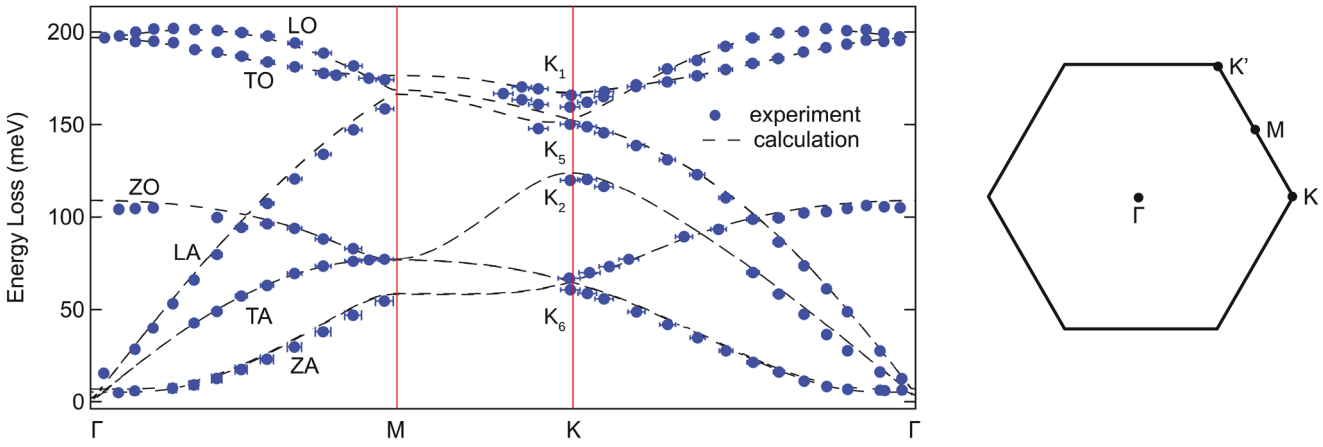

Figure 1. Graphene phonon dispersion along symmetry directions of the Brillouin zone. Left: Phonon dispersion branches of graphene on Ir(111) measured with angle-resolved electron energy loss spectroscopy.[13] ZA (ZO): out-of-plane acoustic (optical); TA (LA): transverse (longitudinal) acoustic; TO (LO): transverse (longitudinal) optical. K_i ($i = 1, 2, 5, 6$) denotes the graphene eigenmodes at **K**. Reproduced with permission.[13] Copyright 2013, American Physical Society. Right: Graphene Brillouin zone with indicated high-symmetry points. $|\Gamma M| = 2\pi/(\sqrt{3}a) = 0.148\ \text{nm}^{-1}$; $|\Gamma K| = 4\pi/(3a) = 0.171\ \text{nm}^{-1}$; $a = 0.245$ nm (graphene lattice constant on Ir(111)).

Figure 2 introduces the example of a single layer of graphene prepared on Ir(111) using the thermal decomposition of C_2H_4. The low-energy electron diffraction pattern of the surface (Figure 2a) exhibits a hexagonal array of satellite spots around each Ir(111) substrate diffraction peak, which is due to the moiré pattern of uniformly oriented incommensurate graphene.[59] The moiré superstructure is the result of the lattice mismatch between graphene and Ir(111) and reflects a spatial beating pattern. A direct consequence of the additional periodic superstructure imposed by the moiré lattice is the backfolding of the electron and phonon band structure, which gives rise to minibands[60,61] and replica of phonon dispersion branches.[14]

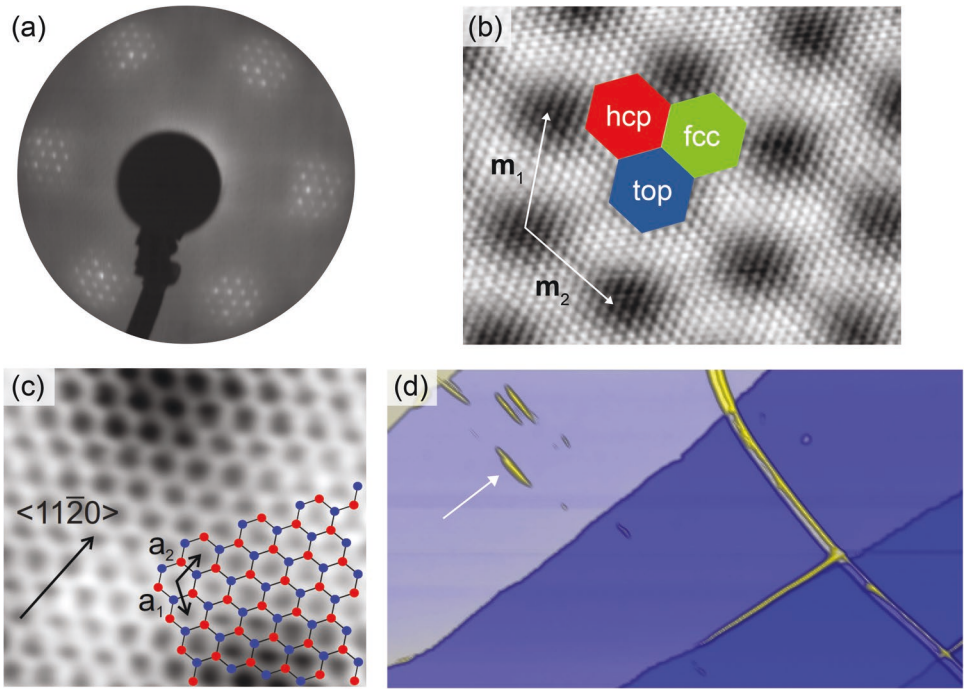

Figure 2. Graphene on Ir(111): diffraction patterns and scanning tunneling microscopy images. a) Low-energy electron diffraction pattern of graphene-covered Ir(111) (kinetic energy of impinging electrons: 147 eV). Reproduced with permission.[13] Copyright 2013, American Physical Society. b) Atomically resolved STM image of graphene (tunneling current: 200 nA; bias voltage: 40 mV; size: 9 nm × 7 nm) showing the moiré superlattice as a periodic modulation of the apparent height of the atomic graphene lattice. The moiré unit cell is spanned by $\mathbf{m}_1$, $\mathbf{m}_2$. The indicated regions depict the different stacking geometry of graphene on Ir(111), i. e., C atoms residing close to on-top positions of Ir(111) atoms, face-centered cubic (fcc), and hexagonal close-packed (hcp) substrate lattice sites. c) STM image of the honeycomb C lattice with indicated lattice vectors $\mathbf{a}_1$, $\mathbf{a}_2$ and crystallographic orientation (3 nA; 12 mV; 2.5 nm × 2.2 nm). d) STM image of graphene-covered Ir(111) (100 pA; 100 mV; 350 nm × 190 nm). The arrow marks a wrinkle. Reproduced with permission.[37] Copyright 2017, American Physical Society.

Figure 2b shows an STM image of graphene on Ir(111), where the moiré pattern is visible in real space with vectors $\mathbf{m}_1$, $\mathbf{m}_2$ ($|\mathbf{m}_1| = |\mathbf{m}_2| \approx 2.5$ nm) spanning the moiré lattice unit cell. The different apparent heights of the moiré lattice are due to C hexagons of the graphene lattice (Figure 2c) residing at or close to specific Ir(111) sites.[62] The brightest contrast reflects C hexagons of the graphene mesh encircling face-centered cubic (fcc) Ir(111) lattice sites (green hexagon in Figure 2b), while the protrusion with less contrast is due to graphene regions, where C hexagons encircle hexagonal close-packed (hcp) Ir(111) lattice sites (red hexagon in Figure 2b). Consequently, the geometrically higher top regions (blue hexagon in Figure 2b) of the moiré lattice appear lower in STM images than the geometrically lower fcc and hcp regions, which is in agreement with previous observations[56] and was traced to particular features in the electronic structure.[62]

The honeycomb C lattice appears in a close-up view (Figure 2c) together with an illustration of the C atom arrangement with graphene lattice vectors $\mathbf{a}_1$, $\mathbf{a}_2$ ($|\mathbf{a}_1| = |\mathbf{a}_2| \approx 0.25$ nm). The orientation of the graphene zig-zag direction, $\langle 11\bar{2}0 \rangle$, co-in-cides here with a close-packed direction of the Ir(111) substrate, $\langle 1\bar{1}0 \rangle$.

Figure 2d presents a large-scale STM image of graphene-covered Ir(111) with graphene nanostructures that become important for the IETS of graphene phonons (vide infra). The nanostructures adopt the form of wrinkles and blisters and represent graphene that is locally delaminated from the Ir(111) surface. They occur upon cooling the freshly prepared graphene sheet from elevated (>1400 K) to room temperature due to the mismatch in thermal expansion coefficients of graphene and Ir(111).[63] The different methods for graphene preparation on metal surfaces—mainly segregation and thermal decomposition—were thoroughly reviewed previously.[64]

Another major method for graphene preparation is the thermal decomposition of SiC.[65–67] SiC surfaces annealed at elevated temperature (>1300 K) under vacuum were demonstrated to exhibit the propensity toward graphitization.[65,68] Crystalline graphite forms on SiC(0001) starting with a first graphene sheet growing on top of the Si-terminated SiC(0001) surface giving rise to characteristic and coexisting $(6\sqrt{3}\times 6\sqrt{3})\mathrm{R}30^\circ$, $(\sqrt{3}\times\sqrt{3})\mathrm{R}30^\circ$ superstructures,[69] which are referred to as the buffer layer (BL)[70–73] or C nanomesh.[74] In the course of higher annealing, the $(\sqrt{3}\times\sqrt{3})\mathrm{R}30^\circ$ superstructure vanishes and the second graphene layer grows on top of the buffer layer, reveals a $(6\sqrt{3}\times 6\sqrt{3})\,\mathrm{R}\,30^\circ$ coincidence lattice, and is very weakly coupled to the SiC substrate. The interface between the SiC substrate and the buffer layer is characterized by C—Si covalent bonds or C, Si dangling bonds leading to interfacial electronic states that are affected by the local atomic environment.[72,75,76] Previous density functional calculations demonstrated that dangling bonds of C and Si atoms at the BL–SiC(0001) interface form band structures around the Fermi level.[75] Importantly, owing to the interaction of graphene with the BL and SiC(0001), the interfacial electronic structure impacts the atom-specific local density of states (DOS) of graphene, as shown for the atomically resolved local DOS of p_z components of graphene C atoms.[75]

Metal carbide surfaces, such as WC(0001),[77] were likewise used for graphene growth. However, graphene phonons have not been reported in IETS experiments so far and, consequently, these surfaces are not the focus of this review article. The reader is referred to an overview of available data on graphene-covered metal carbide surfaces.[78]

Table 1. Collection of surfaces with the most appropriate preparation methods of single-layer graphene. C deposition: exposure of the sample surface to a C atom beam; segregation: thermally activated diffusion of C from the bulk to the surface; decomposition: thermal decomposition of a hydrocarbon molecule on the (catalytically active) heated surface; decomposition*: thermal breaking of Si—C bonds on SiC(0001); cleavage: mechanical breaking of the substrate in a plane perpendicular to the surface normal; exfoliation: transfer of a graphene sheet (possibly of several C layers) from a graphite substrate to the target surface.

Surface	Method	Refs.
Ag(111)	C deposition	[79]
Au(111)	C deposition	[80]
Co(0001)	Segregation	[52]
Cu(111)	Decomposition	[81–85]
HOPG	Cleavage	[32]
Ir(111)	Decomposition	[54–57, 60]
Ni(111)	Segregation	[49,51]
	Decomposition	[86–99]
Ni(100)	Segregation	[50]
	Decomposition	[100]
Pd(111)	Segregation	[52]
Pd(100)	Segregation	[52]
Pt(111)	Segregation	[45,47]
	Decomposition	[101–108]
Pt(110)	Segregation	[45,47]
Pt(100)	Segregation	[44–47]
	Decomposition	[103]
Re(0001)	Decomposition	[109]
Rh(111)	Segregation	[110]
Rh(100)	Decomposition	[110]
Ru(0001)	Segregation	[48,111–115]
	Decomposition	[113,116–120]
SiC(0001)	Decomposition*	[65–68]
SiO_2	Exfoliation	[1]

Table 1 summarizes a few sample surfaces together with the most appropriate preparation method of single-layer graphene. The collection of data is based on a similar table presented previously,[64] extended by semimetal, semiconductor, and insulator surfaces. The dominant preparation methods are the transfer of graphene via exfoliation from a graphite substrate to the target surface and the epitaxial growth using chemical vapor deposition (exposure to hydrocarbon molecules and their decomposition upon adsorption on a heated metal surface, exposure to atomic C) or thermally activated C segregation from the bulk to the surface. Some substrates, e. g., Ag(111) and Au(111), require their exposure to a beam of atomic C for graphene growth. On semiconducting and insulating surfaces, exfoliated single-layer graphene exhibits its virtually genuine free-standing electronic structure, which is favorable for many physical studies. However, the number of graphene sheets is hardly controlled in this production process and additional

analysis tools, e. g., Raman spectroscopy, have to be used to determine the number of graphene layers.

In contrast, a surface science approach to single-layer graphene is achieved by the ultrahigh-vacuum epitaxial growth of the C mesh on metal surfaces with no propensity for C segregation. Moreover, depending on the graphene–metal combination, the coupling of graphene to the substrate can be tuned to some extent. Indeed, a strong hybridization of graphene with a metal surface is indicated by a small graphene–surface distance of 210–220 pm. In this case, the characteristic π band electronic structure is severely modified and a bandgap opens. Prominent examples for the strong-coupling limit are Co and Ni, where the C lattice exhibits registry with the underlying metal lattice. Other metal surfaces with strong coupling to graphene are Re, Rh, and Ru. However, in contrast to Co and Ni, the C lattice on Re, Rh, and Ru does not register with the substrate lattice. Rather, a strongly corrugated moiré superlattice forms where the largest (smallest) graphene–surface distance is 360–380 pm (≈210 pm). Therefore, these graphene-covered surfaces offer the unique opportunity to study physical properties depending on the local degree of the graphene–metal hybridization, which is particularly attractive for atomically resolved microscopy and spectroscopy experiments. An overall weak hybridization with an average graphene–surface distance of ≈330 pm is observed from Ir and Pt. Graphene on these surfaces shows an essentially unperturbed π band with a nearly intact Dirac cone at the **K**-point of the BZ.

2.2. Inelastic Electron Tunneling Spectroscopy—A Primer

In IET, the tunneling electron transfers energy to quantum excitations, such as photons,[121] vibrations,[122] and spin flips.[123] The IET process and its fingerprint in I–V characteristics of the tunneling junction is schematically illustrated in **Figure 3**. Tip and sample are considered as metals at 0 K for simplicity and are represented by their electronic states filled up to the respective Fermi levels, $E_F^{(t)}$ and $E_F^{(s)}$ (Figure 3a). A positive bias voltage ($V > 0$ V) raises $E_F^{(t)}$ by eV (e: elementary charge) relative to $E_F^{(s)}$ and enables a net tunneling current across the vacuum barrier, which can be approximated as electron tunneling through a one-dimensonal (1D) trapezoidal barrier.[124] For small V, i. e., $|eV| \ll \Phi^{(t)}, \Phi^{(s)}$ ($\Phi^{(t)}$, $\Phi^{(s)}$: tip and sample work functions), a purely elastic tunneling current gives rise to a nearly linear I–V behavior (Figure 3b). An inelastic excitation with energy ε becomes possible for electron energies $|eV| \geqslant \varepsilon$; that is, the I–V characteristics are subject to changes in their slopes at the threshold voltages $V = \pm\varepsilon/e$. Very often, IET spectra are presented in the form of dI/dV or d^2I/dV^2 as a function of V, where the changes in the I–V slope occur as, respectively, step-like or peak-like features at $\pm\varepsilon/e$.

The first report on excitation and detection of single-molecule vibrations[122] opened the avenue to chemical identification of adsorbates with an STM. C_2H_2 and C_2D_2 molecules on Cu(100) that appeared essentially identical in constant-current STM images were unambiguously discriminated by the different energies of C–H and C–D stretch modes. This seminal study also showed that the spectroscopic signal strength is low, several percent of dI/dV variation at most. In addition, not all possible vibrational modes appear in the IET spectrum. Only

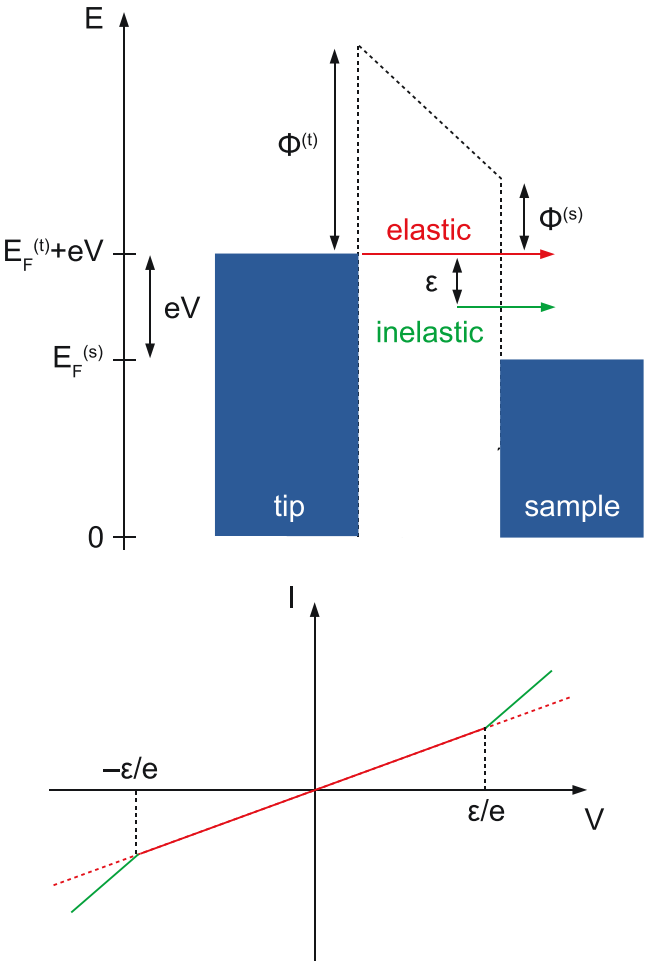

Figure 3. Schematics of inelastic electron tunneling spectroscopy. Top: Illustration of elastic and inelastic electron tunneling through a 1D trapezoidal barrier. The Fermi levels of the tip, $E_F^{(t)}$, and of the sample, $E_F^{(s)}$, differ by eV (e: elementary charge; V: bias voltage) to enable a net tunneling current from occupied states of the tip to unoccupied states of the sample. $\Phi^{(t)}$ and $\Phi^{(s)}$ denote the work function of, respectively, tip and sample. Elastic tunneling electrons reach the sample states without energy loss and thermalize in the sample; inelastic tunneling electrons loose energy ε due to quantum excitation in the tunneling barrier. Bottom: Idealized dependence of the current I on V for the tunneling junction in the top panel where at bias voltage $\pm\varepsilon/e$, $I(V)$ changes the slope due to the opening of the additional inelastic electron transport channel.

the C–H (C–D) stretch mode left its fingerprint in IET spectra. A later work demonstrated that in the course of quantum excitation, a decrease rather than an increase of the junction dI/dV may occur.[125] These observations cannot be explained within the simple model of IET depicted in Figure 3. Rather, propensity or approximate selection rules[126–129] have to be considered in order to appropriately take the symmetry of electronic and vibrational structure of both adsorbate and substrate into account. An immediate consequence of this more sophisticated approach is the impact of vibrational excitations on the elastic current as well. Upon exceeding the threshold voltage virtual excitations, i. e., the emission and absorption of quanta in a time $\tau \approx \hbar/\varepsilon$ ($\hbar = h/(2\pi)$, h: Planck constant) given by the

Heisenberg uncertainty relation, occur. Unlike real excitations, the virtual quanta can give rise to a decrease of dI/dV,[126] which, occasionally, can compensate the dI/dV increase due to the excitation of real quanta and, consequently, are the cause for their disappearance from the IET spectra.

Exceptions to the low change in dI/dV due to vibration excitation occur when IET is resonantly enhanced.[130–135] To this end, a molecular resonance close to E_F is directly involved in the tunneling process, which increases both the tunneling DOS and the electron–vibration coupling. A particularly beautiful example was previously reported for C_{60} on Pb(111), where all Jahn–Teller active H_g modes contribute to the IET spectrum.[132] Later, it was experimentally demonstrated that the spectral overlap of orbital and vibrational energies has a profound influence on the spectroscopic line shape of the molecular vibrational quantum.[134,135] Another mechanism leading to a strongly enhanced IETS signal is the phonon-mediated tunneling process (vide infra).

More than two decades after the first report of single-molecule IETS with an STM,[122] a wealth of vibrational spectra of single atoms and molecules adsorbed on a variety of surfaces has been published. Excellent review articles summarize these results.[136–141] In contrast, IETS of lattice vibrations has very scarcely been reported so far. Phonons of graphite,[142] $Bi_2Sr_2CaCu_2O_{8+\delta}$,[143] Au(111),[144,145] Ag(100),[146] thin Pb films on Cu(111),[147] and Cu(110)[148] were previously measured using STM-IETS. Only recently, a theoretical work has described the STM-IETS of surface phonons of Cu(110) using a nonequilibrium Green's function method.[149]

Experimentally, the most convenient way to extract dI/dV or d^2I/dV^2 from the measured I–V characteristics is the use of a lock-in amplifier. To this end, the bias voltage is modulated by an ac voltage δV with angular frequency ω and the current response of the junction is phase-sensitively detected. For $|\delta V| \ll V$, the nth harmonic of the current response is proportional to $d^{(n)}I/dV^{(n)}$; that is, for dI/dV and d^2I/dV^2 the lock-in amplifier has to be locked at ω and 2ω, respectively. Finite δV leads to the broadening of spectroscopic line shapes, which for detailed studies of IETS data has to be taken into account.[134,135,150–152] A thorough overview of the lock-in amplifier principles and applications is available.[153]

3. Results and Discussion

This section summarizes the experimental results of IETS of graphene phonons on a variety of surfaces. The most appealing common observation on the majority of surfaces is the exceptionally high spectroscopic phonon signal strength. In the model section of this paragraph, the actual signal strength observed in the IET spectra will be traced to the graphene phonon DOS, the electron–phonon coupling strength, and the graphene–electrode hybridization. Choosing graphene–surface combinations with substrates ranging from insulators via semiconductors and semimetals to metals, the hybridization can be tuned and its effect on the phonon signal strength accessed. The influence of the second electrode, the metal tip, can be scrutinized by changing the tip–surface distance from far tunneling separations to the contact range. The experimental data will likewise evidence the importance of the graphene–substrate interface for the observation of graphene phonon signatures in IETS.

3.1. Graphene on Semiconducting Surfaces

3.1.1. SiC(0001)

Monolayer and bilayer graphene on SiC(0001) exhibit a gap in dI/dV spectra symmetrically positioned around zero bias voltage.[25] Its first observation was tentatively interpreted as a phonon-induced gap. Later on, the proposed phonon scenario was confirmed for graphene on *n*-doped 6H-SiC(0001)[26,27] by showing that out-of-plane acoustic phonons with energies of 16, 70, and 140 meV contribute to the electron transport. The gap is particularly pronounced at surface regions where localized states are present at the graphene–SiC(0001) interface.[26,27] The localized states increase the inelastic tunneling current up to approximately one half of the elastic current. Other spectroscopy results, in contrast, do not indicate the presence of graphene phonon signatures on SiC(0001).[154,155]

More recently, a combined STM-IETS and density functional theory (DFT) study showed for graphene on *n*-doped 4H-SiC(0001) that different phonon modes contribute to the IET spectra, albeit with different signal strengths depending on the surface site at which the spectrum is recorded.[29] Low-energy (9 meV) phonons were attributed to vibrations in graphene, while excitations at higher energy (24 meV) were assigned to interfacial Si phonon modes.

These conflicting results concerning the absence or presence of graphene phonon signatures as well as the actual phonon mode visible in the IET spectrum may hint at the importance of the quality of the graphene–substrate interface for the presence or absence of graphene and interfacial phonon modes.

3.1.2. SiO_2

Monolayer graphene was exfoliated on an ≈300 nm thick SiO_2 film on a strongly doped Si crystal.[30,31] This stacking enabled the gating of graphene and, thus, tunable changes in the graphene charge carrier density, i. e., in the energy of the Dirac point, E_D. Spectroscopy of dI/dV as a function of the gate voltage led to an observation that was essential for proposing the phonon-mediated tunneling mechanism. The evolution of E_D with the gate voltage revealed an offset of E_D by half of the width of a dI/dV gap around zero bias voltage. This observation was interpreted as the inelastic tunneling to the graphene Dirac point induced by phonon excitation with an energy matching the E_D offset. Appropriate graphene phonon modes were identified as the out-of-plane acoustic phonons at **K** and **K′** of the graphene BZ.

The phonon-mediated tunneling mechanism works as follows. Electrons with energies smaller than **K**-point phonon energies tunnel elastically into graphene. Final states for these electrons are available at **K** and **K′** only. Due to the involved finite wave vector parallel to the graphene plane ($|\Gamma\mathbf{K}| = 0.171\ \mathrm{nm}^{-1}$; Figure 1), the elastic tunneling process is exponentially suppressed.[156] However, once the threshold

energy is reached, tunneling into **K** and **K′** states is enhanced by the opening of an inelastic transport channel. The electron is subject to a virtual transition to the graphene unoccupied diffuse states at the BZ **Γ**-point,[157] which are here denoted by σ, and reaches the π-band with energy close to E_F at **K** and **K′** by the emission of a phonon with wave vector $\mathbf{q} = \mathbf{K} = \mathbf{K}'$. In other words, the strong enhancement of the tunneling current is due to the mixing of the σ-band and the π-band due to an out-of-plane acoustic phonon mode at **K** and **K′**.[158]

3.1.3. h-BN-Covered SiO_2

Graphene on h-BN-covered SiO_2 with a doped Si back gate enabled the mapping of large parts of the graphene phonon DOS with IETS by adjusting the total charge carrier density.[34] A variety of graphene phonons with wave vectors at **Γ**, **M**, and **K** of the BZ together with, presumably, overtone modes were observed in gate-averaged spectra. In the gate-averaging method, all dI/dV spectra acquired in the full range of applied gate voltages are averaged and presented as a single spectrum. A pertinent question arises as to the apparent difference of graphene on SiO_2, discussed in the previous section. Why do many graphene phonons occur in IET spectra of graphene on h-BN-covered SiO_2, which contrasts the single **K**-point phonon for graphene on SiO_2? Most likely, the h-BN sheet induces a small lattice deformation of graphene, thereby breaking its perfect lattice symmetry. Such deformations were previously demonstrated in a theoretical work[158] to induce band mixing between electronic states at the corners (**K**, **K′**)—which are required as final states for the inelastic tunneling electrons—and other parts of the BZ, which owing to the phonon-mediated tunneling mechanism[30] results in an enhancement of the tunneling DOS at various phonon threshold energies.

The actual IETS signal strength of a graphene phonon was moreover traced to the charge carrier character that was globally tuned by the gate voltage and locally by the STM tip.[34] When the graphene charge carrier is switched—electron to hole or vice versa—the phonon signal is resonantly enhanced. The joint action of gate voltage and the electric field between tip and graphene forms local circular pn junctions that host quasi-bound resonances referred to as whispering gallery modes. Such a resonance acts as an intermediate state for the tunneling electron and gives rise to the phonon signal enhancement as long as the whispering gallery mode is available.

3.2. Graphene on Semimetal Surfaces

3.2.1. Highly Oriented Pyrolytic Graphite (HOPG)

Graphene on HOPG was prepared by cleaving HOPG and spotting single-layer graphene flakes with an STM.[32] The distinctive honeycomb structure of the graphene lattice and the linear variation of the DOS with the bias voltage in dI/dV spectroscopy served as reliable indicators for the presence of single-layer graphene. The excitation of an A_{1g} phonon (LA phonon mode at **K**; Figure 1) at ≈±150 meV was indirectly inferred from the energy dependence of the Fermi velocity, which was obtained from the experimentally extracted electron dispersion relation. Enhanced phonon signatures were not reported in that work.

3.3. Graphene on Metal Surfaces

3.3.1. Ru(0001)

A first hint to graphene phonon excitation in IET with an STM was reported for epitaxially grown graphene on Ru(0001).[42] The observed dI/dV gap around zero bias voltage was traced to a K_6 acoustic phonon (ZA phonon mode at **K**; Figure 1) with energy ≈67 meV. In a later report,[43] signatures in IET spectra appeared at ±360 mV, which were attributed to the second overtone of a graphene optical phonon. Importantly, the signal strength was demonstrated to depend on the lateral position atop the moiré pattern induced by the graphene and Ru(0001) lattice mismatch. In hill regions of the moiré superstructure, the signal strength was lower than at the valley sites, which was assigned to the spatial variation of the electron–phonon interaction.

Both works[42,43] report the presence of graphene phonon signatures in IET spectra. However, in one case a K_6 phonon[42] and in the other case an optical phonon[43] was reported. This inconsistent picture may be related to the different preparation of the surfaces and hints at the importance of the quality of graphene, Ru(0001), and their interface. Moreover, graphene on Ru(0001) belongs to the strong-coupling limit where the graphene–metal hybridization destroys most of the characteristic properties of graphene.[64] In particular, a nearly undistorted electronic structure of free graphene that is required to drive the phonon-mediated tunneling process is not available.

3.3.2. Pt(111)

Nanobubbles of graphene on Pt(111) with diameters (heights) ranging from 1 to 6 nm (0.1 to 1 nm) were prepared by Ar implantation.[36] Spatially resolved dI/dV spectroscopy across a graphene bubble revealed a zero-bias gap that appeared in its most pronounced form at the very top of the highest bubbles, while it vanished on flat graphene on Pt(111). The symmetrically positioned onsets of the gap were observed at ≈±70 mV and attributed to the excitation of **K**-point out-of-plane acoustic graphene phonons. In that publication,[36] the exact mechanism by which the graphene–Pt interaction affects the phonon signal strength in IETS was not clarified. The reduced graphene–Pt coupling in the nanobubble region was tentatively suggested as the origin of the enhancement of the phonon signal.

3.3.3. Ir(111)

Wrinkles and blisters of graphene on Ir(111) (Figure 2) represent another type of graphene nanostructures in which the graphene–metal interaction is reduced. While on flat graphene IET spectra appear virtually featureless (bottom spectrum of **Figure 4**), increasingly pronounced signatures are observed on the graphene blisters toward their maximum elevation (middle and top spectra).[37] Peaks in d^2I/dV^2 spectra occur at

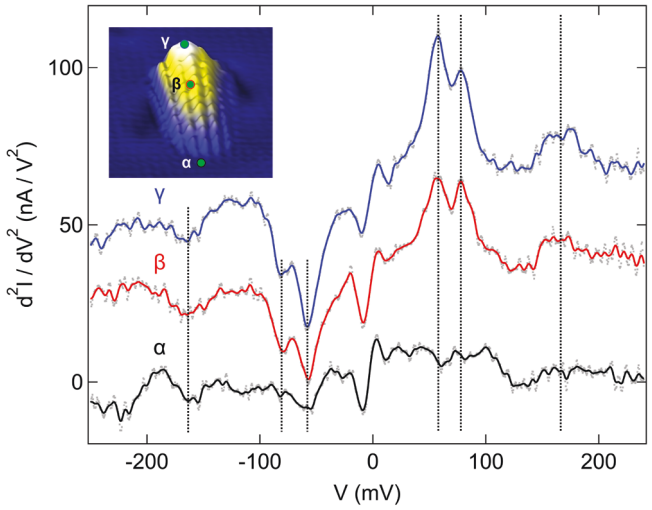

Figure 4. Lateral phonon spectroscopy of graphene wrinkles on Ir(111). Spectra of d^2I/dV^2 acquired atop positions α, β, and γ indicated in the inset. The dashed lines mark the spectroscopic signatures of the ZA phonon at **M** (58 mV), TA and ZO phonons at **M** (77 mV), as well as LA, LO, and ZO phonons at **M**, **K** (150–180 mV). Spectrum β (γ) is vertically offset by 30 nA V^{-2} (60 nA V^{-2}). Feedback loop parameters: 0.1 nA; 250 mV. Inset: Pseudo-3D presentation of STM data of a graphene wrinkle (0.1 nA; 250 mV; 5.3 nm × 5.3 nm). Reproduced with permission.[37] Copyright 2017, American Physical Society.

±57, ±77, and ±165 mV. Using previously reported graphene dispersion branches (Figure 1),[13,14] these peaks were attributed to the ZA phonon at **M** (58 meV), the TA and ZO phonons at **M** (77 meV), as well as to LA, LO, and TO phonon modes covering the broad energy range between 150 and 180 meV at **M** and **K**. Importantly, rather than observing a single peak at the energy of nearly degenerate ZA and ZO phonons at **K**, as previously reported for graphene on SiO_2,[30] a clearly split peak with maxima at 57 and 77 mV was observed in the spectra, which hints at the excitation of ZA and ZO phonons at **M**. Apparently, the observation of **M**-point rather than **K**-point phonons in IETS is at odds with the previously suggested picture of phonon-mediated tunneling and will further be discussed in the section on modeling below.

Another important aspect that was previously not taken into account is the role of the tip in graphene phonon IETS. **Figure 5**a shows the evolution of IET spectra with increasing tip displacement Δz (bottom to top) toward graphene on Ir(111) (Figure 5b). The phonon signatures decrease with increasing Δz and essentially vanish at the tip–graphene contact ($\Delta z = z_c$). Contact is defined by the point of maximum attraction between tip and graphene, which signals a chemical bond and may readily be determined from I–Δz characteristics (Figure 5b), as demonstrated previously for a variety of tips and surfaces.[159–183] For $\Delta z < z_c$, the exponential evolution of I differs from the one observed for $\Delta z > z_c$, and the transition between these two ranges may be abrupt or gradual depending on the contact site.[173] The tip–graphene hybridization obviously has a profound effect on the IET signal strength and will be elaborated below (Section 3.4).

Graphene on Ir(111) was further used to scrutinize the impact of the graphene–substrate coupling on the IETS of

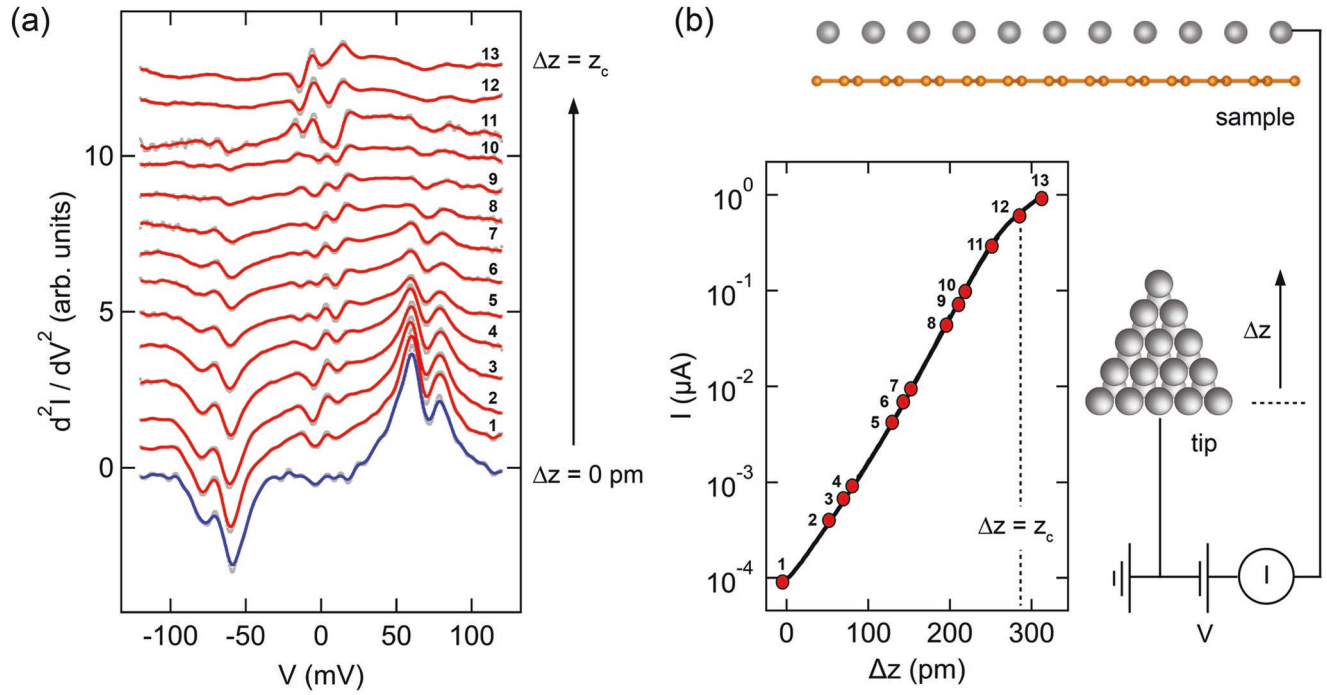

Figure 5. Vertical phonon spectroscopy of graphene wrinkles on Ir(111). a) d^2I/dV^2 spectra recorded above a wrinkle with increasing tip displacement Δz and concomitantly increasing junction conductance $G = I/V$, which ranges from $5\times10^{-6}G_0$ (bottom, $\Delta z = 0$ pm) to $0.1G_0$ (top, $\Delta z = z_c$, z_c: displacement until contact). $G_0 = 2e^2/h$ is the quantum of conductance. The numbering of the individual spectra indicates the current across the junction shown in (b). The spectra were normalized to the current at 120 mV and are vertically offset. Reproduced with permission.[37] Copyright 2017, American Physical Society. b) Schematics of the tunneling junction defining the tip displacement Δz. The current I evolves exponentially with Δz, with a higher rate in the tunneling ($0 \le \Delta z < z_c$, **1**–**11**) than in the contact ($\Delta z \ge \Delta z_c$, **12**, **13**) range.

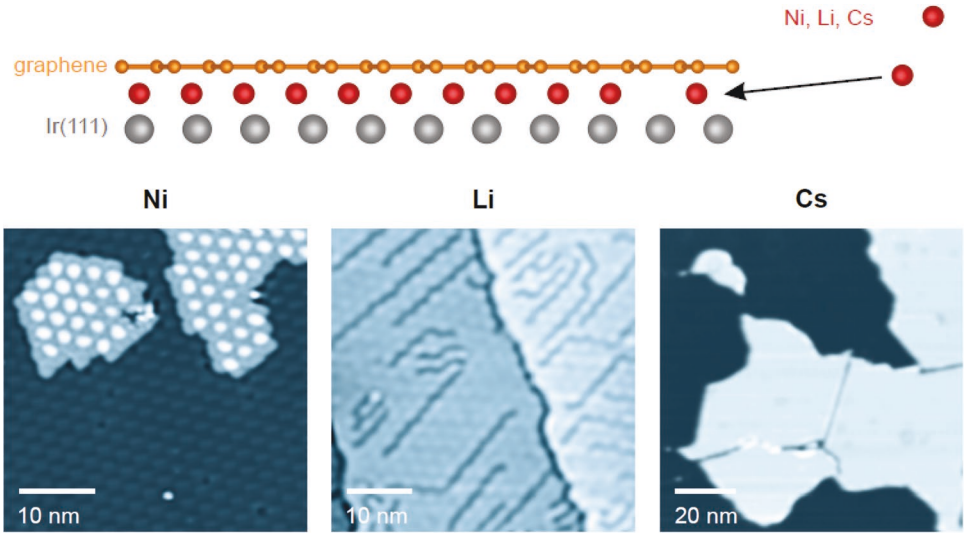

Figure 6. Metal-intercalated graphene on Ir(111). Top: Illustration of the intercalation process. Reproduced with permission.[184] Copyright 2016, American Chemical Society. Bottom: Constant-current STM images (100 pA; 120 mV) of graphene-covered Ir(111) intercalated by Ni (40 nm × 40 nm, left), Li (50 nm × 50 nm, middle), and Cs (100 nm × 100 nm, right). Dark (bright) contrast corresponds to low (high) apparent height. Reproduced with permission.[38] Copyright 2018, American Chemical Society.

graphene phonons. To this end, transition metal Ni as well as alkali metals Cs and Li were intercalated.[38,184] Representative STM images of the intercalated samples are depicted in **Figure 6** together with an illustration of the intercalation process. The presence of the moiré superlattice guides the intercalation of the alkali metals to some extent,[184] which leads to surface structures that deviate from findings obtained for, e. g., alkali metal adsorption on metal surfaces.[185–190]

The corrugation amplitude due to the moiré pattern is largest for the Ni-intercalated sample (105 ± 3 pm), followed by Li-intercalated graphene (9 ± 1 pm). For Cs intercalation the corrugation amplitude stayed below the resolution limit. According to previous works in which the moiré pattern corrugation was identified as a measure of the graphene–substrate hybridization,[191,192] graphene is strongly coupled to the intercalated Ni film, weakly hybridized with Li, and well decoupled from intercalated Cs.

Spectra of $g = \mathrm{d}I/\mathrm{d}V$ normalized to their value at $V = 0$ V, $g(0)$, show a pronounced gap around zero bias voltage for Cs and Li, while it is featureless for Ni (**Figure 7**a). The gap is flanked by abrupt increases of g at ±56 and ±75 mV with a ratio $g/g(0)$ exceeding 200% for Cs and being ≈140% for Li in case of the densely packed alkali metal films, (2×2) Cs and $(\sqrt{3} \times \sqrt{3})\mathrm{R}30^\circ$ Li, respectively. It is worth mentioning that Cs and Li provide similar doping at equal coverage.[193] However, our experiments show that even on the densely packed $(\sqrt{3} \times \sqrt{3})\mathrm{R}30^\circ$ Li film, the IETS intensity is still well below that of the (2×2) Cs-intercalated sample (Figure 7a). Consequently, the charge carrier density alone cannot adequately describe the graphene phonon excitation in IET, which is in disagreement with previous results[30,31,33,34] and demonstrates the necessity of a comprehensive description. To determine the voltages of the gap onsets more reliably, Figure 7b shows the numerical derivative, $\mathrm{d}g/\mathrm{d}V$, of the data presented in Figure 7a. These spectra are very similar to the spectroscopic data obtained for graphene wrinkles on Ir(111) (Figure 4) and, therefore, the peaks are attributed to ZA and ZO phonon excitation at M. As observed for the graphene wrinkles, the phonon modes become efficiently quenched in IET spectra of the intercalated samples upon decreasing the tip–graphene distance (Section 3.4).[38]

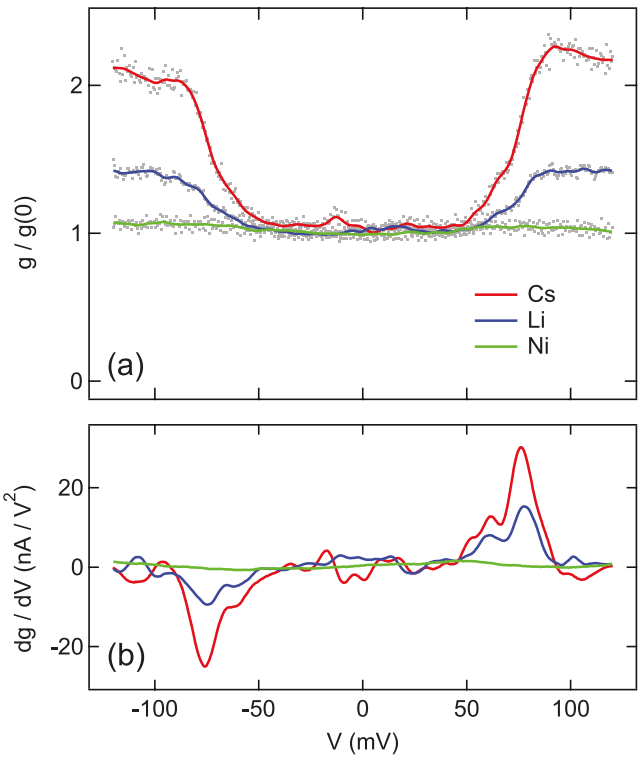

Figure 7. IETS of graphene on Ir(111) intercalated by alkali (Cs, Li) and transition (Ni) metals. a) $g = \mathrm{d}I/\mathrm{d}V$ spectra of the intercalated samples, normalized to the zero-bias differential conductance, $g(0)$. Cs and Li data exhibit step-like signatures that are ascribed to the excitation of graphene phonons, while Ni data are essentially featureless. b) Numerical derivative ($\mathrm{d}g/\mathrm{d}V$) of the spectra in (a). Reproduced with permission.[38] Copyright 2018, American Chemical Society.

3.4. Modeling

To clearly see that modeling of graphene phonon IETS is highly desired, the discrepancies and novelties revealed by the experimental works (vide supra) are briefly summarized.

a) The observation of **M**-point[37,38] rather than **K**-point[30] phonons challenges the picture of phonon-mediated tunneling, for which the **K**-point π-bands close to E_F play the role of final states for the inelastic tunneling electron. At the **M**-point, suitable final states are not available.
b) The difference in IET spectra for the different intercalated metals (Figure 7)[38] requires a quantitative rationale.
c) The hybridization of graphene with the second electrode—the tip—and the resulting suppression of the phonon signals in IETS (Figure 5)[37,38] calls for an explanation.
d) Graphene on SiO_2 exhibits extraordinarily high phonon signals in IETS,[30] although reports are available that contradict these results by the absence of phonon-related signatures.[40,41]
e) For graphene on SiC(0001), dI/dV data show[25–27,29] and do not show[154,155] a phonon-induced gap. In the case of the presence of phonon signatures in the spectra, the actual phonon modes contributing to dI/dV are not the same.
f) The comparison of graphene on Ru(0001) and graphene on Ir(111), Pt(111) is particularly challenging in the following sense. Graphene on Ru(0001) is a prominent example for the strong graphene–metal hybridization.[64] The characteristic graphene electronic structure is severely distorted[116,117] and, therefore, deviates appreciably from its free-standing behavior. As a consequence, the observed phonon signatures in IETS[42,43] are surprising from the perspective of the phonon-mediated tunneling process that requires the (nearly) intact graphene electronic structure. In contrast, graphene on Ir(111) and Pt(111) exhibits a weakly distorted genuine band structure.[60,194] However, phonon signatures stay below the detection limit in IETS on these surfaces. Only in case of delaminated graphene nanostructures on these surfaces strong phonon signals were reported.[36,37]

Issue (a) will be addressed by evaluating the role of the phonon DOS in IETS, while an answer to issues (b)–(f) will be provided on the basis of the graphene hybridization with the metal surface and the tip.

3.4.1. Importance of the Phonon Density of States

In a theoretical effort to understand the contribution of **M**-point phonons to IET spectra (point (a) of the open issues listed above), the momentum-resolved and energy-resolved spectral function $A(q, E)$ was calculated.[37] Using a Green's function formalism for a nearly free electron gas with energy E_σ it was previously shown that

$$A(q,E) \approx -\frac{\Im\Sigma(q,E)}{\pi E_\sigma^2} \propto \Im\Sigma(q,E) \tag{1}$$

with $\Im\Sigma(q, E)$ the imaginary part of the self-energy $\Sigma(q, E)$, which describes the electron–phonon coupling according to

$$\Sigma(q,E) \approx -\pi\lambda^2 \sum_j \Theta(|E| - \hbar\omega_{j,\pm K+q}) N^\pi[E - \mathrm{sgn}(E)\hbar\omega_{j,\pm K+q}] \tag{2}$$

where λ is the electron–phonon coupling parameter, Θ the Heaviside function, $N^\pi(E) \approx \alpha|E + \mu|$ the nearly linear DOS of the graphene π-bands for energies relative to the chemical potential μ, and $\hbar\omega_{j,\pm K+q}$ the energy of a ZA, ZO phonon branch j with wave vector $\pm K + q$ ($K = |\Gamma\mathbf{K}| = 0.171\,\mathrm{nm}^{-1}$; Figure 1). The calculations are constrained to the out-of-plane phonon modes ZA and ZO since they dominantly contribute to the experimental spectra below 100 mV (Figures 4, 5a, and 7).

The Tersoff–Hamann model[156] simplifies the electronic structure of the tip as an s-orbital and shows that dI/dV is proportional to the sample DOS at the s-orbital center for sufficiently small bias voltage. To derive dI/dV, $A(q, E)$ (Equation (1)) has to be weighted by the squared electron wave function $|\Psi_q(z)|^2$ and integrated over the BZ yielding the tunneling DOS

$$A(z,E) = \int_{\mathrm{BZ}} |\Psi_q(z)|^2 A(q,E) \mathrm{d}^2q \tag{3}$$

with $dI/dV \propto A(z, E)$ and $d^2I/dV^2 \propto dA(z, E)/dE$. Using $|\Psi_q(z)|^2 \propto \exp(-\kappa z)$ with decay constant $\kappa = 2\sqrt{\kappa_0^2 + q^2} \approx 2\kappa_0 + q^2/\kappa_0$ shows that electronic states with elevated wave vector q are effectively suppressed. Therefore, the integral in Equation (3) is limited to a range $D(\Gamma) = \{\mathbf{q} \in \mathrm{BZ} : |\mathbf{q}| = q < q_m \equiv \sqrt{\kappa_0/z}\}$ around the Γ-point of the BZ; that is

$$A(z,E) = \int_{D(\Gamma)} A(q,E) \mathrm{d}^2q \tag{4}$$

Therefore, combining Equations (1)–(4) with $E = eV$, one arrives at[37]

$$\frac{\mathrm{d}I}{\mathrm{d}V} \propto A(z,E) \propto \lambda^2 \int \Theta(|E| - \hbar\omega) N^\pi[E - \mathrm{sgn}(E)\hbar\omega] N^{\mathrm{ph}}(\hbar\omega) \mathrm{d}\omega \tag{5}$$

and

$$\frac{\mathrm{d}^2I}{\mathrm{d}V^2} \propto \frac{\mathrm{d}A(z,E)}{\mathrm{d}E} \propto \lambda^2 \cdot \mathrm{sgn}(E) \left[N^\pi(0) N^{\mathrm{ph}}(|E|) + \alpha \int_0^{|E|} N^{\mathrm{ph}}(\hbar\omega) \mathrm{d}\omega \right] \tag{6}$$

where

$$N^{\mathrm{ph}}(\hbar\omega) = \sum_j \int_{D(\mathbf{K})} \delta(\hbar\omega - \hbar\omega_{j,q}) \mathrm{d}^2q \tag{7}$$

$\left(D(\mathbf{K}) = \{\pm\mathbf{K} + \mathbf{q} \in \mathrm{BZ} : |\mathbf{q}| = q < q_m\}\right)$ is the effective graphene phonon DOS.

Figure 8 summarizes the calculated results for $A(z, E)$ (Figure 8a) and $dA(z, E)/dE$ (Figure 8b). The parameters used for the calculations are marked in the legend and listed in the caption. The effective graphene phonon DOS, N^{ph}, was obtained from the calculated dispersion of out-of-plane phonons in the nearest-neighbor approximation[195] with force constants adjusted to qualitatively reproduce the dispersion branches between **M** and **K**. The $A(z, E)$ curves appear with a gap around

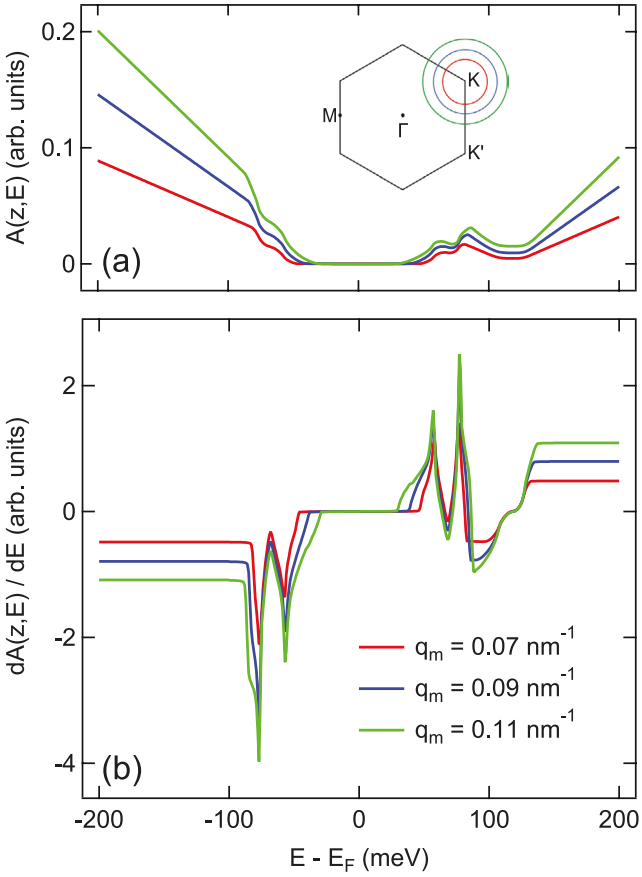

Figure 8. Simulation of free-graphene IET spectra. a) Calculated tunneling DOS $A(z, E)$, Equation (5), and b) IET spectra $dA(z, E)/dE$, Equation (6), for indicated q_m and $\mu = -50$ meV. Inset to (a): Graphene BZ with high symmetry points **Γ**, **K**, **K′**, **M**. The concentric circles indicate the regions of the BZ that enter into the integration to obtain $A(z, E)$. Reproduced with permission.[37] Copyright 2017, American Physical Society.

E_F symmetrically flanked by step-like increases at ±58 meV (ZA) and ±78 meV (ZO), which give rise to dips and peaks in dA/dE, in agreement with the experimental observations. Deviating from previous results where only signatures of degenerate ZA and ZO graphene phonons at **K** were reported in IET spectra,[30] Equation (6) unveils that phonons at **M** with sufficiently high DOS may leave their fingerprint as well. ZA and ZO phonons exhibit a flat dispersion around **M** in the **K**–**M** direction (Figure 1). In particular, the dispersion exhibits saddle points at **M** with energies 58 and 78 meV.[196] These regions are partially covered by the integration disk $D(\mathbf{K})$ (or $D(\mathbf{K}')$) and thus give rise to peaks in $N^{ph}(\hbar\omega)$ at 58 and 78 meV. Increasing q_m mainly broadens the steps of $A(q, E)$ (the peaks of $dA(z, E)/dE$) since phonons with larger wave vectors and different energies contribute to the IET process.

The dips between the IETS peaks may be understood from $N^{ph}(\hbar\omega)$, too. Around **K** and **K′**, the ZA and ZO phonon dispersion is linear and exhibits a conical point at ≈65 meV leading to the ∨-shaped minimum in $N^{ph}(\hbar\omega)$ and to the dips in the IETS signals.

The discussed results nicely show the importance of a high phonon DOS for the presence of elevated graphene phonon signals in IET spectra. It complements the originally proposed phonon-mediated tunneling mechanism. However, these results were obtained for free-standing graphene with its intact characteristic electronic structure. A further improvement in IET modeling is the consideration of the graphene–substrate and graphene–tip hybridization, which will be discussed next.

3.4.2. Branching of the Tunneling Current into Elastic and Inelastic Transport Channels

While the details of the density functional and nonequilibrium Green's function calculations were discussed in extenso in the original publication,[38] a simplified two-level model (**Figure 9**) that illustrates the more complex simulations is reported here. At the heart of the transport calculations is a three-terminal setup, in which the conventional two-terminal setup consisting of tip and substrate is extended by a third terminal that collects electrons propagating in graphene alone. The third terminal reflects graphene self-energies that replace the periodic boundary conditions in the two-terminal configuration by open boundary conditions in one graphene direction. The calculations consider the first unoccupied band σ of graphene with energy E_σ at Γ and a graphene π-state with energy E_F at **K**. The coupling of these states to the metal substrate is modeled by inverse lifetimes, Γ_σ and Γ_π, where $\Gamma_\sigma > \Gamma_\pi$ due to the long range of σ.[157] Additionally, the σ-state is coupled to the tip with Γ_t. Electrons injected from the tip into σ can either directly continue to the substrate, which constitutes the elastic transport

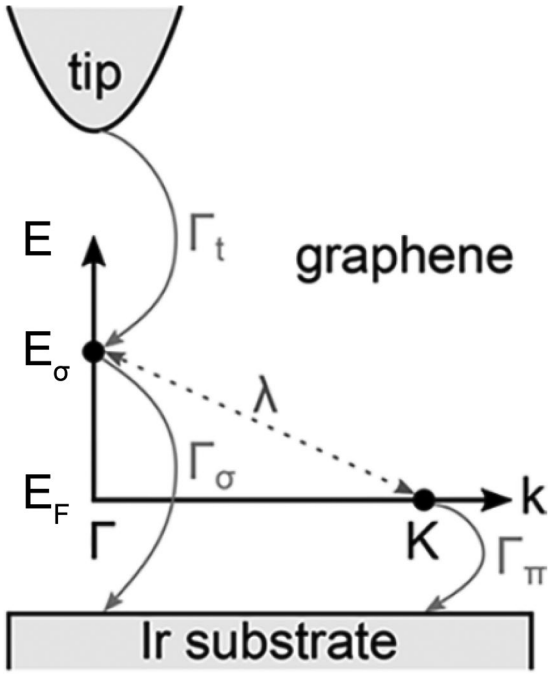

Figure 9. Illustration of electron transport in the three-terminal setup. The tip couples to graphene σ-states with energy E_σ at Γ with a coupling constant Γ_t. The hybridization of graphene to the substrate is mediated by σ-states with strength Γ_σ and by π-states with strength Γ_π. π-states occur at **K** with energy E_F (Fermi energy). σ-states and π-states are coupled by the electron–phonon interaction of strength λ. Reproduced with permission.[38] Copyright 2018, American Chemical Society.

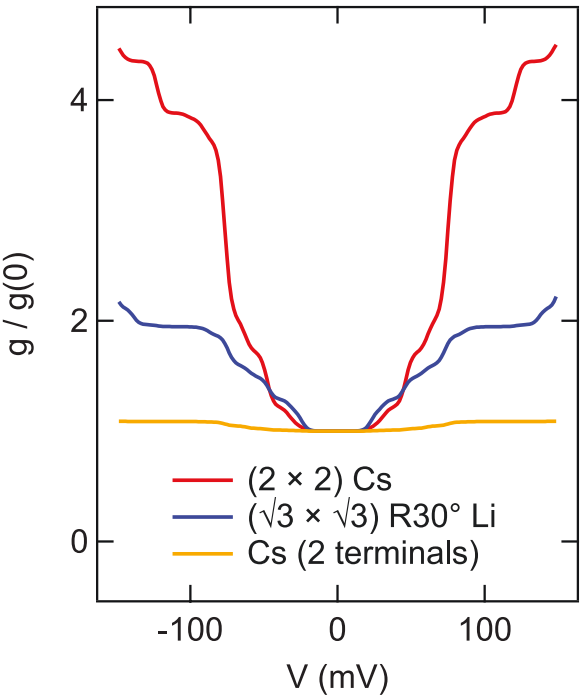

Figure 10. Calculated $g/g(0)$ for graphene on Ir(111) intercalated by (2×2) Cs and $(\sqrt{3}\times\sqrt{3})R30^{\circ}$Li superlattices in the three-terminal setup. In the conventional two-terminal approach (calculated for Cs, bottom curve), IET signals are virtually absent. Reproduced with permission.[38] Copyright 2018, American Chemical Society.

channel, or take the detour via π through electron–phonon coupling with strength λ. In this inelastic transport channel, a phonon with energy $\hbar\Omega$ is excited. For $\hbar\Omega \ll \Gamma_\pi$ in the lowest-order expansion of the electron–phonon coupling and in the wide-band approximation,[197,198] the relative conductance increase due to phonon excitation can be expressed as[38]

$$\frac{\Delta g}{g(0)} \equiv \frac{g-g(0)}{g(0)} = \frac{4\lambda^2}{\Gamma_\pi}\cdot\left(\frac{1}{\Gamma_t}+\frac{1}{\Gamma_\sigma}\right) \tag{8}$$

In the tunneling range, $\Gamma_\sigma \gg \Gamma_t$, Equation (8) may further be simplified to

$$\frac{\Delta g}{g(0)} = \frac{4\lambda^2}{\Gamma_\pi \Gamma_t} \tag{9}$$

Consequently, for similar Γ_t and comparable λ, the IETS signal is controlled by Γ_π.

Can Equations (8) and (9) in principle be used to rationalize the aforementioned issues (b)–(f)?

The success of the simulations is demonstrated in **Figure 10**, where calculated $g/g(0)$ is plotted as a function of the bias voltage. The three-terminal model can qualitatively reproduce the experimental findings. Quantitatively, the same order of magnitude for the phonon-induced changes in $g/g(0)$ is obtained, although they exceed the experimental values. In addition, several phonon excitations are visible in the $g/g(0)$ calculations. The contributing phonon modes in the simulations are similar to the out-of-plane bands at **M** and **K**, but the breaking of symmetry by the substrate also yields contributions shifted away from these. Figure 10 (bottom curve) shows that the conventional two-terminal setup fails in describing the experimental data. Even for the Cs case where the strongest phonon signatures would be expected according to the experiments, inelastic features vanish. Therefore, the branching of the current into the metal substrate and the continuum of graphene states is important to explain the strong phonon signals.

A reduced coupling Γ_π between graphene and the substrate corresponds to a longer lifetime of the π-state, which entails a stronger interaction with graphene phonons and, therefore, enhances the IET signals. This indicates that graphene on the Cs-intercalated samples is less hybridized with the metal than on Li-intercalated samples, which is consistent with the essentially vanishing moiré corrugation of graphene atop the Cs film (Figure 6). In the case of Ni intercalation, the graphene π-bands are strongly hybridized with Ni 3d-bands,[192] which in the simple model is reflected by a large Γ_π. Consequently, the interaction of the π-state with graphene phonons is reduced and renders the inelastic transport channel inefficient. The current, therefore, flows directly into the bulk of the metal substrate via the elastic transport channel. Concomitantly, the phonon signatures disappear from the dI/dV spectra.

Therefore, issue (b) is well described by the different magnitudes of Γ_π in the cases of Cs, Li, and Ni intercalants. The developed model can likewise explain the extraordinarily high IET phonon signals observed from graphene on insulating and semiconducting surfaces,[25,30,31,33,34] graphene blisters on Pt(111)[36] and Ir(111).[37] In these cases, Γ_σ is reduced, too, due to the low hybridization with substrate states at the Fermi level. This scenario yields $\Gamma_\sigma \approx \Gamma_t \approx \Gamma_\pi$ (Equation (8)), which combines efficient inelastic transport with a small elastic current and leads to exceptionally large IET signals.

Not only the impact of the graphene–substrate coupling on the graphene phonon IETS signal strength may be described by the model; from Equations (8) and (9), the influence of the tip coupling Γ_t may be examined as well (issue (c) of the open issues). Experimentally, the relative increase of dI/dV due to phonon excitation is lowered with increasing junction conductance from tunneling to contact ranges, as shown for graphene nanobubbles on Ir(111) (Figure 5a) and for graphene on Ir(111) intercalated by Cs (**Figure 11**a) and Li (Figure 11b). The experimentally observed trends for varying junction conductance are well captured by the simulations (Figure 11c). The phonon-induced gap becomes shallower with increasing junction conductance. At contact (topmost data sets in Figures 5a and 11a–c), the IET signatures of graphene phonons have essentially disappeared.

The observed quenching of $\Delta g/g(0)$ upon tip approach in the experiments as well as in the calculations indicates the dominating role of Γ_t. First, Γ_t increases with tip approach due to the increased van der Waals interaction between tip and graphene.[199,200] Second, according to the model (Figure 9), a larger Γ_t enhances both the elastic and inelastic transport channel. Since $\Gamma_\sigma > \Gamma_\pi \gg \hbar\Omega$, the elastic channel is dominant and the ratio of inelastic and elastic currents decreases, and so does $\Delta g/g(0)$ (Equation (8)). An additional effect leading to the enhancement of both tunneling channels is the gradual lifting of the momentum conservation due to the local symmetry

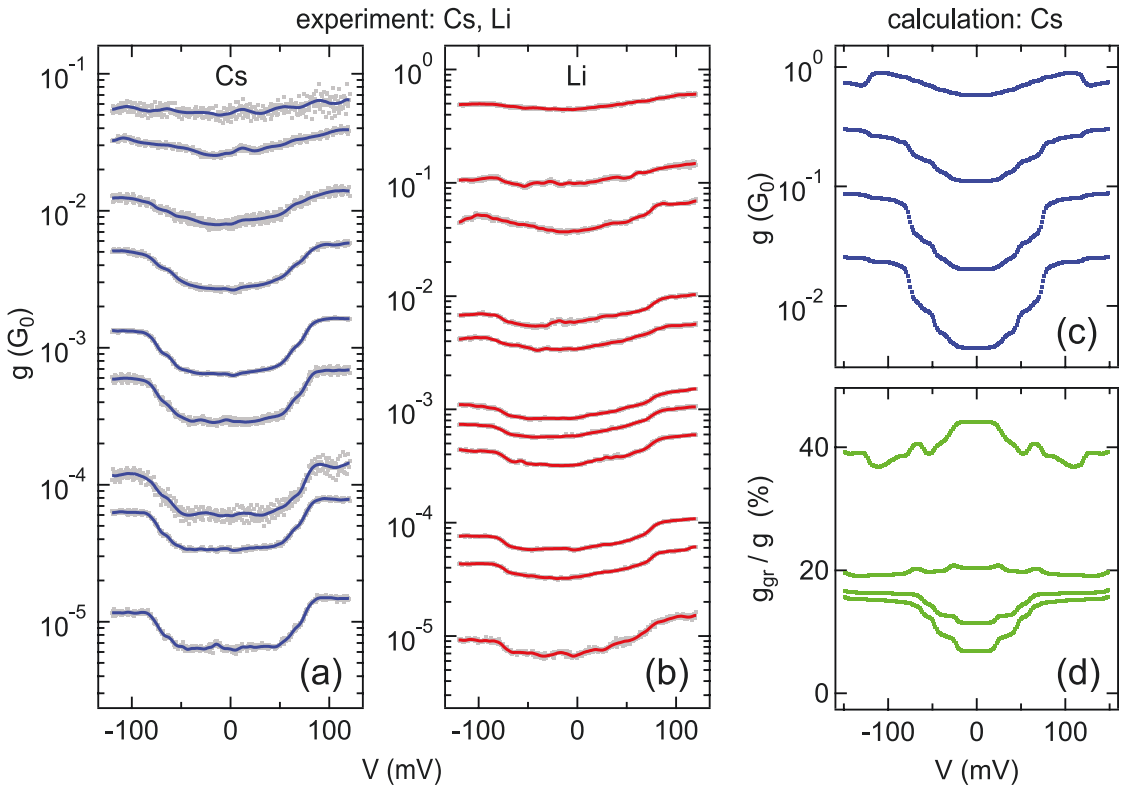

Figure 11. Experimental and calculated IET spectra depending on the tip–graphene distance. a) Experimental dI/dV (g) spectra of Cs-intercalated graphene for increasing (bottom to top) junction conductance showing the progressive quenching of the graphene phonon gap. b) Same as (a) for Li. c) Simulated dI/dV (g) spectra of Cs-intercalated graphene in the three-terminal model for junction conductances of $0.004G_0$, $0.02G_0$, $0.1G_0$, and $0.6G_0$ (bottom to top). d) Relative contribution (g_{Gr}/g) of the graphene terminal to the total calculated differential conductance g for junction conductances as in (c). Reproduced with permission.[38] Copyright 2018, American Chemical Society.

breaking by the approaching tip.[28] Indeed, the contribution of the graphene terminal to the total conductance rapidly rises (Figure 11d). Close to contact, many phonon modes from different regions of the BZ may contribute,[37] which lowers the resolution of distinct phonon signatures in the IETS.

The occasional absence of phonon spectroscopic signatures in dI/dV spectra obtained for exfoliated graphene on SiO_2[40,41] (issue (d)) may be explained by larger values of Γ_σ. Indeed, the graphene–SiO_2 interface is characterized by charged impurities and single-electron charging effects giving rise to a substantial disorder potential.[41] The concomitant breaking of the graphene symmetry in weak-disorder systems leads to Γ_σ dominating Γ_π.[201] For graphene on SiC(000$\bar{1}$), a combination of STM experiments and ab initio calculations showed that the substitution of C by N atoms leads to an enhancement of the elastic electron transport at the N sites due to symmetry breaking.[28] As a consequence, the phonon-mediated inelastic tunneling channel that leads to clear phonon signals in IETS at C sites is inefficient at the N-doped sites. A similar argument was used previously to explain the absence of graphene phonon signals when the STM tip contacts the graphene sheet.[37]

Issues (e) and (f) of the list require further spatially resolved spectroscopies in order to establish a clear-cut relation to the three-terminal model.

For SiC(0001), it was demonstrated that interface states between the C buffer layer and the SiC surface lead to a spatial variation of dI/dV spectra.[154] These interface states result from C dangling bonds of the buffer layer and Si dangling bonds of the SiC substrate with energies matching the graphene phonon energies.[75] At first sight, the localized interface states may be responsible to enhance the elastic transport channel. The concomitantly increased Γ_σ would effectively suppress graphene phonon signatures in IET spectra. However, according to previous findings,[26,27] the graphene phonons are strongly coupled to the localized interface states, which may be translated into a high electron–phonon coupling parameter in the three-terminal model discussed here.[38] A similar line of argument is followed to explain the observation of locally varying phonon-induced gap widths in IET spectra of graphene on SiC(0001).[29] These variations were previously attributed to the presence or absence of the dangling bond at the interfacial Si atom.[29] At present it remains unclear why different phonon modes were reported in these works.[26,27,29]

The observation of graphene phonons on graphene-covered Ru(0001) in IETS at the same time with featureless IET spectra of graphene on Ir(111) and Pt(111)—issue (f) of the list—is more difficult to explain on the basis of Equations (8) and (9). At the time of writing this review article, only preliminary explanations can be provided. Graphene phonons on Ru(0001) appear in IET spectra with spatial variations, which was previously attributed to a site-dependent electron–phonon interaction.[43] Density functional calculations showed that C—Ru chemical

bonds are restricted to the (geometric) minima of the corrugated graphene lattice, while the maxima reflect the absence of chemical bonds.[64] The spatial variations in the chemical bond strengths entails a site-dependent coupling parameter Γ_π, which may be responsible for the alternating weak and strong signals of graphene phonons in IETS.

The absence of phonon signatures on graphene-covered Ir(111) and Pt(111) surfaces may be rationalized in terms of a dominating elastic electron transport channel due to the presence of surface resonances in the center of the BZ. Using dI/dV spectroscopy and density functional calculations, it was previously demonstrated that a hole-like surface resonance of clean Ir(111) with energy ≈–0.35 eV below E_F is subject to a shift to ≈–0.16 eV for graphene-covered Ir(111).[202] Importantly, the gradual appearance of the phonon-induced gap in spatially resolved dI/dV spectra acquired atop increasing elevations of graphene wrinkles and blisters is accompanied by the gradual disappearance of the surface resonance.[37] In other words, tunneling through graphene π-states and emission of phonons becomes progressively dominant at the expense of the elastic transport channel. While similar data have not been available for graphene on Pt(111) to date, an akin picture may hold owing to the presence of a surface resonance close to E_F at the BZ center.[203–205]

3.5. Perspective

Phonon signals of graphene appear in spectroscopy of dI/dV with exceptionally high signal strength. The phonon-mediated tunneling mechanism explains this observation on the basis of a sufficiently preserved genuine electronic structure of graphene, which requires a gap at Γ and some finite DOS at and close to **K** of the BZ. An extension of the phonon-mediated tunneling picture is required in order to rationalize the presence of phonon spectroscopic signatures with wave vectors deviating from **K** and to explain the variety of signal strengths observed from graphene on different surfaces. The former task is addressed by including band mixing due to graphene lattice distortions and the phonon DOS in the description of IETS, while the latter is well captured by considering the graphene–electrode hybridization. With these tools at hand—phonon-mediated tunneling, band mixing, phonon DOS, and graphene–electrode coupling—available graphene phonon IETS data can be described. It will be interesting to apply these tools to stacked graphene sheets and a possible dependence of the graphene phonon signatures in IETS on the twist angle and the local atomic environment defined by the moiré superlattice. Moreover, the presented approach to modeling IETS is likely to apply to other Dirac materials, where quasiparticles with linear dispersion at the BZ corners are coupled through band mixing to higher-energy excitations at the BZ center.

4. Summary and Concluding Remarks

The present work has reviewed the state of the art in STM-IETS of graphene phonons. A variety of substrate surfaces hosting graphene, semiconductor, and semimetal as well as metal surfaces, give rise to enhanced phonon signals in IET spectra. The enhancement is due to a phonon-mediated tunneling process[30] that involves phonons with a sufficiently high DOS.[37] Moreover, the electronic (covalent) coupling of tip and sample to graphene σ-bands and π-bands regulates the current branching across the tunneling junction into elastic and inelastic transport channels, which can explain the observed different extents of enhancements.[38]

The experimental and theoretical findings presented in this work likewise shed light onto the notion of electronic decoupling, which is generally used to characterize the extent of hybridization of an adsorbate with the hosting substrate. The weak hybridization is often attributed to the submolecular resolution in STM images of adsorbed molecules,[206–210] the occurrence of electronic states,[211–219] vibrational quanta,[220–224] and fluorescence photons[225–237] with particularly sharp spectroscopic line shapes. In the case of graphene, the results summarized here are able to provide a more precise and quantitative description of the hybridization. The graphene coupling to the substrate (tip) is characterized by inverse lifetimes Γ_σ and Γ_π (Γ_t), which together with the electron–phonon coupling parameter λ determine the change in dI/dV due to phonon excitation. In particular, weak IET phonon signals are not necessarily related to a strong graphene–substrate coupling; an elevated graphene–tip hybridization or a reduced electron–phonon interaction may as well be the reason.

The combination of IETS data obtained from graphene intercalated by alkali metals with simulations may explain why the predicted Bardeen–Cooper–Schrieffer energy gap[238] has not been observed in spectroscopy of dI/dV. Superconductivity of graphene decorated with Li was previously predicted to set in below a critical temperature of 8.1 K,[238] which is expected to give rise to a superconducting energy gap that would be discernible in dI/dV spectroscopy at an experimental temperature of 5 K. The observation of a pronounced phonon gap rather than the predicted superconductor gap may be rationalized as follows. Spectroscopy of dI/dV probes the tunneling DOS, which in case of a dominant inelastic transport channel shows quantum excitations and suppresses the sheer electronic sample DOS.

Similar phonon enhancement effects have been observed for bilayer graphene[239] and it will be interesting to see the impact of the twist angle on the phonon signal strength in IETS. The rotation angle between the C lattices of top and bottom graphene sheets was previously demonstrated to profoundly impact the electronic structure,[240] which may give rise to modifications in the elastic and inelastic transport channels. Heterogeneous stacking, e. g., graphene on hexagonal boron nitride, are similarly interesting in that respect.

Acknowledgements

Funding by the Deutsche Forschungsgemeinschaft through Grant No. KR 2912/7-1, KR 2912/10-3, KR 2912/12-1, and the research training group 2247 Quantum Mechanical Materials Modelling, by the Danish National Research Foundation through Project DNRF103, and by Villum Fonden through Grant No. 00013340 is acknowledged.

Conflict of Interest

The authors declare no conflict of interest.

Keywords

graphene phonons, inelastic electron tunneling spectroscopy, phonons, scanning tunneling microscopy

Received: November 27, 2019
Revised: January 9, 2020
Published online: March 8, 2020

[1] K. S. Novoselov, A. K. Geim, S. V. Morozov, D. Jiang, Y. Zhang, S. V. Dubonos, I. V. Grigorieva, A. A. Firsov, *Nature* **2004**, *306*, 666.
[2] K. S. Novoselov, A. K. Geim, S. V. Morozov, D. Jiang, M. I. Katsnelson, I. V. Grigorieva, S. V. Dubonos, A. A. Firsov, *Nature* **2005**, *438*, 197.
[3] Y. Zhang, Y.-W. Tan, H. L. Stormer, P. Kim, *Nature* **2005**, *438*, 201.
[4] K. S. Novoselov, D. Jiang, F. Schedin, T. J. Booth, V. V. Khotkevich, S. V. Morozov, A. K. Geim, *Proc. Natl. Acad. Sci. USA* **2005**, *102*, 10451.
[5] Z. Yao, C. L. Kane C. Dekker, *Phys. Rev. Lett.* **2000**, *84*, 2941.
[6] A. Javey, J. Guo, M. Paulsson, Q. Wang, D. Mann, M. Lundstrom, H. Dai, *Phys. Rev. Lett.* **2004**, *92*, 106804.
[7] A. Barreiro, M. Lazzeri, J. Moser, F. Mauri, A. Bachtold, *Phys. Rev. Lett.* **2009**, *103*, 076601.
[8] D. L. Nika, A. A. Balandin, *Rep. Prog. Phys.* **2017**, *80*, 036502.
[9] A. C. Ferrari, J. C. Meyer, V. Scardaci, C. Casiraghi, M. Lazzeri, F. Mauri, S. Piscanec, D. Jiang, K. S. Novoselov, S. Roth, A. K. Geim, *Phys. Rev. Lett.* **2006**, *97*, 187401.
[10] A. C. Ferrari, *Solid State Commun.* **2007**, *143*, 47.
[11] L. Malard, M. Pimenta, G. Dresselhaus, M. Dresselhaus, *Phys. Rep.* **2009**, *473*, 51.
[12] A. Politano, A. R. Marino, V. Formoso, G. Chiarello, *Carbon* **2012**, *50*, 734.
[13] M. Endlich, A. Molina-Sánchez, L. Wirtz, J. Kröger, *Phys. Rev. B* **2013**, *88*, 205403.
[14] M. Endlich, H. P. C. Miranda, A. Molina-Sánchez, L. Wirtz, J. Kröger, *Ann. Phys.* **2014**, *526*, 372.
[15] A. Politano, F. de Juan, G. Chiarello, H. A. Fertig, *Phys. Rev. Lett.* **2015**, *115*, 075504.
[16] A. Politano, *Crit. Rev. Solid State Mater. Sci.* **2017**, *42*, 99.
[17] S. Piscanec, M. Lazzeri, F. Mauri, A. C. Ferrari, J. Robertson, *Phys. Rev. Lett.* **2004**, *93*, 185503.
[18] A. Allard, L. Wirtz, *Nano Lett.* **2010**, *10*, 4335.
[19] F. Fromm, M. H. Oliveira Jr, A. Molina-Sńchez, M. Hundhausen, J. M. J. Lopes, H. Riechert, L. Wirtz, T. Seyller, *New J. Phys.* **2013**, *15*, 043031.
[20] H. Ibach, *J. Electron Spectrosc. Relat. Phenom.* **1993**, *64*, 819.
[21] L. Wirtz, A. Rubio, *Solid State Commun.* **2004**, *131*, 141.
[22] M. Lazzeri, C. Attaccalite, L. Wirtz, F. Mauri, *Phys. Rev. B* **2008**, *78*, 081406.
[23] J. Maultzsch, S. Reich, C. Thomsen, H. Requardt, P. Ordejón, *Phys. Rev. Lett.* **2004**, *92*, 075501.
[24] A. Grüneis, J. Serrano, A. Bosak, M. Lazzeri, S. L. Molodtsov, L. Wirtz, C. Attaccalite, M. Krisch, A. Rubio, F. Mauri, T. Pichler, *Phys. Rev. B* **2009**, *80*, 085423.
[25] V. W. Brar, Y. Zhang, Y. Yayon, T. Ohta, J. L. McChesney, A. Bostwick, E. Rotenberg, K. Horn, M. F. Crommie, *Appl. Phys. Lett.* **2007**, *91*, 122102.
[26] J. Červenka, K. van de Ruit, C. F. J. Flipse, *Phys. Rev. B* **2010**, *81*, 205403.
[27] J. Červenka, K. van de Ruit, C. F. J. Flipse, *Phys. Status Solidi B* **2010**, *247*, 2992.
[28] J. Lagoute, F. Joucken, V. Repain, Y. Tison, C. Chacon, A. Bellec, Y. Girard, R. Sporken, E. H. Conrad, F. Ducastelle, M. Palsgaard, N. P. Andersen, M. Brandbyge, S. Rousset, *Phys. Rev. B* **2015**, *91*, 125442.
[29] E. Minamitani, R. Arafune, T. Frederiksen, T. Suzuki, S. M. F. Shahed, T. Kobayashi, N. Endo, H. Fukidome, S. Watanabe, T. Komeda, *Phys. Rev. B* **2017**, *96*, 155431.
[30] Y. Zhang, V. W. Brar, F. Wang, C. Girit, Y. Yayon, M. Panlasigui, A. Zettl, M. F. Crommie, *Nat. Phys.* **2008**, *4*, 627.
[31] V. W. Brar, S. Wickenburg, M. Panlasigui, C.-H. Park, T. O. Wehling, Y. Zhang, R. Decker, Ç. Girit, A. V. Balatsky, S. G. Louie, A. Zettl, M. F. Crommie, *Phys. Rev. Lett.* **2010**, *104*, 036805.
[32] G. Li, A. Luican, E. Y. Andrei, *Phys. Rev. Lett.* **2009**, *102*, 176804.
[33] R. Decker, Y. Wang, V. W. Brar, W. Regan, H.-Z. Tsai, Q. Wu, W. Gannett, A. Zettl, M. F. Crommie, *Nano Lett.* **2011**, *11*, 2291.
[34] F. D. Natterer, Y. Zhao, J. Wyrick, Y.-H. Chan, W.-Y. Ruan, M.-Y. Chou, K. Watanabe, T. Taniguchi, N. B. Zhitenev, J. A. Stroscio, *Phys. Rev. Lett.* **2015**, *114*, 245502.
[35] S.-Y. Li, K.-K. Bai, W.-J. Zuo, Y.-W. Liu, Z.-Q. Fu, W.-X. Wang, Y. Zhang, L.-J. Yin, J.-B. Qiao, L. He, *Phys. Rev. Appl.* **2018**, *9*, 054031.
[36] H. W. Kim, W. Ko, J. Ku, I. Jeon, D. Kim, H. Kwon, Y. Oh, S. Ryu, Y. Kuk, S. W. Hwang, H. Suh, *Nat. Commun.* **2015**, *6*, 7528.
[37] N. Néel, C. Steinke, T. O. Wehling, J. Kröger, *Phys. Rev. B* **2017**, *95*, 161410.
[38] J. Halle, N. Néel, M. Fonin, M. Brandbyge, J. Kröger, *Nano Lett.* **2018**, *18*, 5697.
[39] E. E. Vdovin, A. Mishchenko, M. T. Greenaway, M. J. Zhu, D. Ghazaryan, A. Misra, Y. Cao, S. V. Morozov, O. Makarovsky, T. M. Fromhold, A. Patanè, G. J. Slotman, M. I. Katsnelson, A. K. Geim, K. S. Novoselov, L. Eaves, *Phys. Rev. Lett.* **2016**, *116*, 186603.
[40] A. Deshpande, W. Bao, F. Miao, C. N. Lau, B. J. LeRoy, *Phys. Rev. B* **2009**, *79*, 205411.
[41] S. Jung, G. M. Rutter, N. N. Klimov, D. B. Newell, I. Calizo, A. R. Walker, N. B. Zhitenev, J. A. Stroscio, *Nat. Phys.* **2011**, *7*, 245.
[42] E. Sutter, D. P. Acharya, J. T. Sadowski, P. Sutter, *Appl. Phys. Lett.* **2009**, *94*, 133101.
[43] A. Castellanos-Gomez, G. Rubio-Bollinger, S. Barja, M. Garnica, A. L. Vázquez de Parga, R. Miranda, N. Agraït, *Appl. Phys. Lett.* **2013**, *102*, 063114.
[44] S. Hagstrom, H. B. Lyon, G. A. Somorjai, *Phys. Rev. Lett.* **1965**, *15*, 491.
[45] H. B. Lyon, G. A. Somorjai, *J. Chem. Phys.* **1967**, *46*, 2539.
[46] A. Morgan, G. Somorjai, *Surf. Sci.* **1968**, *12*, 405.
[47] J. W. May, *Surf. Sci.* **1969**, *17*, 267.
[48] J. Grant, T. Haas, *Surf. Sci.* **1970**, *21*, 76.
[49] J. Shelton, H. Patil, J. Blakely, *Surf. Sci.* **1974**, *43*, 493.
[50] L. Isett, J. Blakely, *Surf. Sci.* **1976**, *58*, 397.
[51] M. Eizenberg, J. Blakely, *Surf. Sci.* **1979**, *82*, 228.
[52] J. Hamilton, J. Blakely, *Surf. Sci.* **1980**, *91*, 199.
[53] S. Helveg, C. López-Cartes, J. Sehested, P. L. Hansen, B. S. Clausen, J. R. Rostrup-Nielsen, F. Abild-Pedersen, J. K. Nørskov, *Nature* **2004**, *427*, 426.
[54] B. Nieuwenhuys, D. Hagen, G. Rovida, G. Somorjai, *Surf. Sci.* **1976**, *59*, 155.
[55] A. T. N'Diaye, S. Bleikamp, P. J. Feibelman, T. Michely, *Phys. Rev. Lett.* **2006**, *97*, 215501.
[56] A. T. N'Diaye, J. Coraux, T. N. Plasa, C. Busse, T. Michely, *New J. Phys.* **2008**, *10*, 043033.
[57] J. Coraux, A. T. N'Diaye, C. Busse, T. Michely, *Nano Lett.* **2008**, *8*, 565.
[58] J. Halle, A. Mehler, N. Néel, J. Kröger, *Phys. Chem. Chem. Phys.* **2019**, *21*, 3140.

[59] H. Hattab, A. T. N'Diaye, D. Wall, G. Jnawali, J. Coraux, C. Busse, R. van Gastel, B. Poelsema, T. Michely, F.-J. M. zu Heringdorf, M. H. von Hoegen, *Appl. Phys. Lett.* **2011**, *98*, 141903.
[60] I. Pletikosić, M. Kralj, P. Pervan, R. Brako, J. Coraux, A. T. N'Diaye, C. Busse, T. Michely, *Phys. Rev.Lett.* **2009**, *102*, 056808.
[61] J. Sánchez-Barriga, A. Varykhalov, D. Marchenko, M. R. Scholz, O. Rader, *Phys. Rev. B* **2012**, *85*, 201413.
[62] E. N. Voloshina, E. Fertitta, A. Garhofer, F. Mittendorfer, M. Fonin, A. Thissen, Y. S. Dedkov, *Sci. Rep.* **2013**, *3*, 1072.
[63] A. T. N'Diaye, R. van Gastel, A. J. Martínez-Galera, J. Coraux, H. Hattab, D. Wall, F.-J. M. zu Heringdorf, M. H. von Hoegen, J. M. Gómez-Rodríguez, B. Poelsema, C. Busse, T. Michely, *New J. Phys.* **2009**, *11*, 113056.
[64] J. Wintterlin, M.-L. Bocquet, *Surf. Sci.* **2009**, *603*, 1841.
[65] I. Forbeaux, J.-M. Themlin, J.-M. Debever, *Phys. Rev. B* **1998**, *58*, 16396.
[66] C. Berger, Z. Song, T. Li, X. Li, A. Y. Ogbazghi, R. Feng, Z. Dai, A. N. Marchenkov, E. H. Conrad, P. N. First, W. A. de Heer, *J. Phys. Chem. B* **2004**, *108*, 19912.
[67] T. Ohta, A. Bostwick, T. Seyller, K. Horn, E. Rotenberg, *Science* **2006**, *313*, 951.
[68] A. V. Bommel, J. Crombeen, A. V. Tooren, *Surf. Sci.* **1975**, *48*, 463.
[69] C. Riedl, U. Starke, J. Bernhardt, M. Franke, K. Heinz, *Phys. Rev. B* **2007**, *76*, 245406.
[70] A. Bostwick, T. Ohta, J. L. McChesney, K. V. Emtsev, T. Seyller, K. Horn, E. Rotenberg, *New J. Phys.* **2007**, *9*, 385.
[71] S. Y. Zhou, G.-H. Gweon, A. V. Fedorov, P. N. First, W. A. de Heer, D.-H. Lee, F. Guinea, A. H. Castro Neto, A. Lanzara, *Nat. Mater.* **2007**, *6*, 770.
[72] A. Mattausch, O. Pankratov, *Phys. Rev. Lett.* **2007**, *99*, 076802.
[73] F. Varchon, R. Feng, J. Hass, X. Li, B. N. Nguyen, C. Naud, P. Mallet, J.-Y. Veuillen, C. Berger, E. H. Conrad, L. Magaud, *Phys. Rev. Lett.* **2007**, *99*, 126805.
[74] W. Chen, H. Xu, L. Liu, X. Gao, D. Qi, G. Peng, S. C. Tan, Y. Feng, K. P. Loh, A. T. S. Wee, *Surf. Sci.* **2005**, *596*, 176.
[75] M. Kajihara, T. Suzuki, S. Shahed, T. Komeda, E. Minamitani, S. Watanabe, *Surf. Sci.* **2016**, *647*, 39.
[76] S. Kim, J. Ihm, H. J. Choi, Y.-W. Son, *Phys. Rev. Lett.* **2008**, *100*, 176802.
[77] P. M. Stefan, M. L. Shek, I. Lindau, W. E. Spicer, L. I. Johansson, F. Herman, R. V. Kasowski, G. Brogen, *Phys. Rev. B* **1984**, *29*, 5423.
[78] M. Batzil, *Surf. Sci. Rep.* **2012**, *67*, 83.
[79] B. Kiraly, E. V. Iski, A. J. Mannix, B. L. Fisher, M. C. Hersam, N. P. Guisinger, *Nat. Commun.* **2013**, *4*, 2804.
[80] J. M. Wofford, E. Starodub, A. L. Walter, S. Nie, A. Bostwick, N. C. Bartelt, K. Thürmer, E. Rotenberg, K. F. McCarty, O. D. Dubon, *New J. Phys.* **2012**, *14*, 053008.
[81] W. Bao, F. Miao, Z. Chen, H. Zhang, W. Jang, C. Dames, C. N. Lau, *Nat. Nanotechnol.* **2009**, *4*, 562.
[82] X. Li, W. Cai, J. An, S. Kim, J. Nah, D. Yang, R. Piner, A. Velamakanni, I. Jung, E. Tutuc, S. K. Banerjee, L. Colombo, R. S. Ruoff, *Science* **2009**, *324*, 1312.
[83] K. S. Kim, Y. Zhao, H. Jang, S. Y. Lee, J. M. Kim, K. S. Kim, J.-H. Ahn, P. Kim, J.-Y. Choi, B. H. Hong, *Nature* **2009**, *457*, 706.
[84] X. Li, W. Cai, L. Colombo, R. S. Ruoff, *Nano Lett.* **2009**, *9*, 4268.
[85] L. Gao, J. R. Guest, N. P. Guisinger, *Nano Lett.* **2010**, *10*, 3512.
[86] R. Rosei, M. De Crescenzi, F. Sette, C. Quaresima, A. Savoia, P. Perfetti, *Phys. Rev. B* **1983**, *28*, 1161.
[87] R. Rosei, S. Modesti, F. Sette, C. Quaresima A. Savoia, P. Perfetti, *Phys. Rev. B* **1984**, *29*, 3416.
[88] A. M. Shikin, G. V. Prudnikova, V. K. Adamchuk, F. Moresco, K.-H. Rieder, *Phys. Rev. B* **2000**, *62*, 13202.
[89] T. Aizawa, R. Souda, Y. Ishizawa, H. Hirano, T. Yamada, K.-i. Tanaka, C. Oshima, *Surf. Sci.* **1990**, *237*, 194.
[90] A. M. Shikin, D. Farías, K. H. Rieder, *Europhys. Lett.* **1998**, *44*, 44.
[91] D. Farías, A. M. Shikin, K.-H. Rieder, *J. Phys.: Condens. Matter* **1999**, *11*, 8453.
[92] D. Farías, K. H. Rieder, A. Shikin, V. Adamchuk, T. Tanaka, C. Oshima, *Surf. Sci.* **2000**, *454–456*, 437.
[93] A. Nagashima, N. Tejima, C. Oshima, *Phys. Rev. B* **1994**, *50*, 17487.
[94] Y. S. Dedkov, M. Fonin, U. Rüdiger, C. Laubschat, *Phys. Rev. Lett.* **2008**, *100*, 107602.
[95] Y. S. Dedkov, M. Fonin, U. Rüdiger, C. Laubschat, *Appl. Phys. Lett.* **2008**, *93*, 022509.
[96] Y. S. Dedkov, A. M. Shikin, V. K. Adamchuk, S. L. Molodtsov, C. Laubschat, A. Bauer, G. Kaindl, *Phys. Rev. B* **2001**, *64*, 035405.
[97] Y. S. Dedkov, M. Fonin, C. Laubschat, *Appl. Phys. Lett.* **2008**, *92*, 052506.
[98] H. Yang, *Surf. Sci.* **1995**, *343*, 61.
[99] H. Kawanowa, H. Ozawa, T. Yazaki, Y. Gotoh, R. Souda, *Jpn. J. Appl. Phys.* **2002**, *41*, 6149.
[100] C. McConville, D. Woodruff, S. Kevan, *Surf. Sci.* **1986**, *171*, L447.
[101] K. Baron, D. Blakely, G. Somorjai, *Surf. Sci.* **1974**, *41*, 45.
[102] H. Zi-Pu, D. Ogletree, M. V. Hove, G. Somorjai, *Surf. Sci.* **1987**, *180*, 433.
[103] B. Lang, *Surf. Sci.* **1975**, *53*, 317.
[104] T. Aizawa, Y. Hwang, W. Hayami, R. Souda, S. Otani, Y. Ishizawa, *Surf. Sci.* **1992**, *260*, 311.
[105] T. Land, T. Michely, R. Behm, J. Hemminger, G. Comsa, *Surf. Sci.* **1992**, *264*, 261.
[106] M. Sasaki, Y. Yamada, Y. Ogiwara, S. Yagyu, S. Yamamoto, *Phys. Rev. B* **2000**, *61*, 15653.
[107] H. Ueta, M. Saida, C. Nakai, Y. Yamada, M. Sasaki, S. Yamamoto, *Surf. Sci.* **2004**, *560*, 183.
[108] D. Starr, E. Pazhetnov, A. Stadnichenko, A. Boronin, S. Shaikhutdinov, *Surf. Sci.* **2006**, *600*, 2688.
[109] E. Miniussi, M. Pozzo, A. Baraldi, E. Vesselli, R. R. Zhan, G. Comelli, T. O. Menteş, M. A. Niño, A. Locatelli, S. Lizzit, D. Alfè, *Phys. Rev. Lett.* **2011**, *106*, 216101.
[110] D. Castner, B. Sexton, G. Somorjai, *Surf. Sci.* **1978**, *71*, 519.
[111] S. Marchini, S. Günther, J. Wintterlin, *Phys. Rev. B* **2007**, *76*, 075429.
[112] P. Yi, S. Dong-Xia, G. Hong-Jun, *Chin. Phys.* **2007**, *16*, 3151.
[113] A. L. Vázquez de Parga, F. Calleja, B. Borca, M. C. G. Passeggi, J. J. Hinarejos, F. Guinea, R. Miranda, *Phys. Rev. Lett.* **2008**, *100*, 056807.
[114] Y. Pan, H. Zhang, D. Shi, J. Sun, S. Du, F. Liu, H.-j. Gao, *Adv. Mater.* **2009**, *21*, 2777.
[115] P. W. Sutter, J.-I. Flege, E. A. Sutter, *Nat. Mater.* **2008**, *7*, 406.
[116] F. Himpsel, K. Christmann, P. Heimann, D. Eastman, P. J. Feibelman, *Surf. Sci.* **1982**, *115*, L159.
[117] T. Brugger, S. Günther, B. Wang, J. H. Dil, M.-L. Bocquet, J. Osterwalder, J. Wintterlin, T. Greber, *Phys. Rev. B* **2009**, *79*, 045407.
[118] J. Hrbek, *J. Vac. Sci. Technol. A* **1994**, *4*, 86.
[119] M.-C. Wu, Q. Xu, D. W. Goodman, *J. Phys. Chem.* **1994**, *98*, 5104.
[120] D. Martoccia, P. R. Willmott, T. Brugger, M. Björck, S. Günther, C. M. Schlepütz, A. Cervellino, S. A. Pauli, B. D. Patterson, S. Marchini, J. Wintterlin, W. Moritz, T. Greber, *Phys. Rev. Lett.* **2008**, *101*, 126102
[121] R. Berndt, R. Gaisch, J. K. Gimzewski, B. Reihl, R. R. Schlittler, W. D. Schneider, M. Tschudy, *Science* **1993**, *262*, 1425.
[122] B. C. Stipe, M. A. Rezaei, W. Ho, *Science* **1998**, *280*, 1732.
[123] A. J. Heinrich, J. A. Gupta, C. P. Lutz, D. M. Eigler, *Science* **2004**, *306*, 466.
[124] J. G. Simmons, *J. Appl. Phys.* **1963**, *34*, 1793.
[125] J. R. Hahn, W. Ho, *Phys. Rev. B* **2009**, *80*, 165428.
[126] N. Lorente, M. Persson, *Phys. Rev. Lett.* **2000**, *85*, 2997.
[127] N. Lorente, M. Persson, L. J. Lauhon, W. Ho, *Phys. Rev. Lett.* **2001**, *86*, 2593.

[128] A. Gagliardi, G. C. Solomon, A. Pecchia, T. Frauenheim, A. Di Carlo, N. S. Hush, J. R. Reimers, *Phys. Rev. B* **2007**, *75*, 174306.
[129] M. Paulsson, T. Frederiksen, H. Ueba, N. Lorente, M. Brandbyge, *Phys. Rev. Lett.* **2008**, *100*, 226604.
[130] B. N. J. Persson, A. Baratoff, *Phys. Rev. Lett.* **1987**, *59*, 339.
[131] M. Galperin, A. Nitzan, M. A. Ratner, *Phys. Rev. B* **2006**, *73*, 045314.
[132] K. J. Franke, G. Schulze, J. I. Pascual, *J. Phys. Chem. Lett.* **2010**, *1*, 500.
[133] K. J. Franke, J. I. Pascual, *J. Phys.: Condens. Matter* **2012**, *24*, 394002.
[134] S. Meierott, N. Néel, J. Kröger, *J. Phys. Chem. Lett.* **2016**, *7*, 2388.
[135] S. Meierott, N. Néel, J. Kröger, *Phys. Rev. B* **2017**, *96*, 205437.
[136] W. Ho, *J. Chem. Phys.* **2002**, *117*, 11033.
[137] N. Lorente, R. Rurali, H. Tang, *J. Phys.: Condens. Matter* **2005**, *17*, S1049.
[138] S.-W. Hla, *J. Vac. Sci. Technol. B* **2005**, *23*, 1351.
[139] M. Galperin, M. A. Ratner, A. Nitzan, *J. Phys.: Condens. Matter* **2007**, *19*, 103201.
[140] K. Morgenstern, N. Lorente, K.-H. Rieder, *Phys. Status Solidi B* **2013**, *250*, 1671.
[141] S. You, J.-T. Lü, J. Guo, Y. Jiang, *Adv. Phys.: X* **2017**, *2*, 907.
[142] L. Vitali, M. A. Schneider, K. Kern, L. Wirtz, A. Rubio, *Phys. Rev. B* **2004**, *69*, 121414.
[143] J. Lee, K. Fujita, K. McElroy, J. A. Slezak, M. Wang, Y. Aiura, H. Bando, M. Ishikado, T. Masui, J.-X. Zhu, A. V. Balatsky, H. Eisaki, S. Uchida, J.-C. Davis, *Nature* **2006**, *442*, 546.
[144] H. Gawronski, M. Mehlhorn, K. Morgenstern, *Science* **2008**, *319*, 930.
[145] I. Altfeder, A. A. Voevodin, A. K. Roy, *Phys. Rev. Lett.* **2010**, *105*, 166101.
[146] K. Volgmann, H. Gawronski, C. Zaum, G. G. Rusina, S. D. Borisova, E. V. Chulkov, K. Morgenstern, *Nat. Commun.* **2014**, *5*, 5089.
[147] M. Schackert, T. Märkl, J. Jandke, M. Hölzer, S. Ostanin, E. K. U. Gross, A. Ernst, W. Wulfhekel, *Phys. Rev. Lett.* **2015**, *114*, 047002.
[148] E. Minamitani, R. Arafune, N. Tsukahara, Y. Ohda, S. Watanabe, M. Kawai, H. Ueba, N. Takagi, *Phys. Rev. B* **2016**, *93*, 085411.
[149] E. Minamitani, N. Takagi, R. Arafune, T. Frederiksen, T. Komeda, H. Ueba, S. Watanabe, *Prog. Surf. Sci.* **2018**, *93*, 131.
[150] P. Echenique, R. Berndt, E. Chulkov, T. Fauster, A. Goldmann, U. Höfer, *Surf. Sci. Rep.* **2004**, *52*, 219.
[151] J. Kröger, L. Limot, H. Jensen, R. Berndt, S. Crampin, E. Pehlke, *Prog. Surf. Sci.* **2005**, *80*, 26.
[152] J. Kröger, M. Becker, H. Jensen, T. von Hofe, N. Néel, L. Limot, R. Berndt, S. Crampin, E. Pehlke, C. Corriol, V. Silkin, D. Sánchez-Portal, A. Arnau, E. Chulkov, P. Echenique, *Prog. Surf. Sci.* **2007**, *82*, 293.
[153] M. L. Maede, *Lock-in Amplifiers: Principles and Applications*, Peter Peregrinus Ltd., London, UK **1983**.
[154] G. M. Rutter, N. P. Guisinger, J. N. Crain, E. A. A. Jarvis, M. D. Stiles, T. Li, P. N. First, J. A. Stroscio, *Phys. Rev. B* **2007**, *76*, 235416.
[155] S. Nie, R. M. Feenstra, *J. Vac. Sci. Technol. A* **2009**, *27*, 1052.
[156] J. Tersoff, D. R. Hamann, *Phys. Rev. Lett.* **1983**, *50*, 1998.
[157] N. R. Papior, G. Calogero, M. Brandbyge, *J. Phys.: Condens. Matter* **2018**, *30*, 25LT01.
[158] T. O. Wehling, I. Grigorenko, A. I. Lichtenstein, A. V. Balatsky, *Phys. Rev. Lett.* **2008**, *101*, 216803.
[159] N. Agraït, A. L. Yeyati, J. M. van Ruitenbeek, *Phys. Rep.* **2003**, *377*, 81.
[160] L. Limot, J. Kröger, R. Berndt, A. Garcia-Lekue, W. A. Hofer, *Phys. Rev. Lett.* **2005**, *94*, 126102.
[161] N. Néel, J. Kröger, L. Limot, R. Berndt, *Nanotechnology* **2006**, *18*, 044027.
[162] N. Néel, J. Kröger, L. Limot, K. Palotas, W. A. Hofer, R. Berndt, *Phys. Rev. Lett.* **2007**, *98*, 016801.
[163] N. Néel, J. Kröger, L. Limot, T. Frederiksen, M. Brandbyge, R. Berndt, *Phys. Rev. Lett.* **2007**, *98*, 065502.
[164] J. Kröger, H. Jensen, R. Berndt, *New J. Phys.* **2007**, *9*, 153.
[165] N. Néel, L. Limot, J. Kröger, R. Berndt, *Phys. Rev. B* **2008**, *77*, 125431.
[166] J. Kröger, N. Néel, L. Limot, *J. Phys.: Condens. Matter* **2008**, *20*, 223001.
[167] N. Néel, J. Kröger, L. Limot, R. Berndt, *Nano Lett.* **2008**, *8*, 1291.
[168] N. Néel, J. Kröger, R. Berndt, E. Pehlke, *Phys. Rev. B* **2008**, *78*, 233402.
[169] N. Néel, J. Kröger, R. Berndt, *Phys. Rev. Lett.* **2009**, *102*, 086805.
[170] J. Kröger, N. Néel, A. Sperl, Y. F. Wang, R. Berndt, *New J. Phys.* **2009**, *11*, 125006.
[171] R. Berndt, J. Kröger, N. Néel, G. Schull, *Phys. Chem. Chem. Phys.* **2010**, *12*, 1022.
[172] Y. F. Wang, J. Kröger, R. Berndt, H. Vázquez, M. Brandbyge, M. Paulsson, *Phys. Rev. Lett.* **2010**, *104*, 176802.
[173] S. J. Altenburg, J. Kröger, B. Wang, M.-L. Bocquet, N. Lorente, R. Berndt, *Phys. Rev. Lett.* **2010**, *105*, 236101.
[174] N. Néel, J. Kröger, R. Berndt, *Phys. Rev. B* **2010**, *82*, 233401.
[175] M. Ziegler, N. Néel, C. Lazo, P. Ferriani, S. Heinze, J. Kröger, R. Berndt, *New J. Phys.* **2011**, *13*, 085011.
[176] N. Néel, J. Kröger, R. Berndt, *Nano Lett.* **2011**, *11*, 3593.
[177] N. L. Schneider, N. Néel, N. P. Andersen, J. T. Lü, M. Brandbyge, J. Kröger, R. Berndt, *J. Phys.: Condens. Matter* **2015**, *27*, 015001.
[178] J. Schöneberg, F. Otte, N. Néel, A. Weismann, Y. Mokrousov, J. Kröger, R. Berndt, S. Heinze, *Nano Lett.* **2016**, *16*, 1450.
[179] M. Müller, C. Salgado, N. Néel, J. J. Palacios, J. Kröger, *Phys. Rev. B* **2016**, *93*, 235402.
[180] J. Brand, P. Ribeiro, N. Néel, S. Kirchner, J. Kröger, *Phys. Rev. Lett.* **2017**, *118*, 107001.
[181] M. R. Calvo, C. Sabater, W. Dednam, E. B. Lombardi, M. J. Caturla, C. Untiedt, *Phys. Rev. Lett.* **2018**, *120*, 076802.
[182] C. Sabater, W. Dednam, M. R. Calvo, M. A. Fernández, C. Untiedt, M. J. Caturla, *Phys. Rev. B* **2018**, *97*, 075418.
[183] J. Brand, S. Gozdzik, N. Néel, J. L. Lado, J. Fernández-Rossier, J. Kröger, *Phys. Rev. B* **2018**, *97*, 195429.
[184] J. Halle, N. Néel, J. Kröger, *J. Phys. Chem. C* **2016**, *120*, 5067.
[185] R. D. Diehl, R. McGrath, *Surf. Sci. Rep.* **1996**, *23*, 43.
[186] T. Aruga, T. Hiroshi, M. Yoshitada, *Surf. Sci.* **1986**, *175*, L725.
[187] H. Tochihara, S. Mizuno, *Surf. Sci.* **1992**, *279*, 89.
[188] N. Fischer, S. Schuppler, T. Fauster, W. Steinmann, *Surf. Sci.* **1994**, *314*, 89.
[189] T. von Hofe, J. Kröger, R. Berndt, *Phys. Rev. B* **2006**, *73*, 245434.
[190] M. Ziegler, J. Kröger, R. Berndt, A. Filinov, M. Bonitz, *Phys. Rev. B* **2008**, *78*, 245427.
[191] A. B. Preobrajenski, M. L. Ng, A. S. Vinogradov, N. Mårtensson, *Phys. Rev. B* **2008**, *78*, 073401.
[192] D. Pacilé, P. Leicht, M. Papagno, P. M. Sheverdyaeva, P. Moras, C Carbone, K. Krausert, L. Zielke, M. Fonin, Y. S. Dedkov, F. Mittendorfer, J. Doppler, A. Garhofer, J. Redinger, *Phys. Rev. B* **2013**, *87*, 035420.
[193] M. Andersen, L. Hornekær, B. Hammer, *Phys. Rev. B* **2014**, *90*, 155428.
[194] I. I. Klimovskikh, M. M. Otrokov, V. Y. Voroshnin, D. Sostina, L. Petaccia, G. Di Santo, S. Thakur, E. V. Chulkov, A. M. Shikin, *ACS Nano* **2017**, *11*, 368.
[195] L. A. Falkovsky, *J. Exp. Theor. Phys.* **2007**, *105*, 397.
[196] O. Dubay, G. Kresse, *Phys. Rev. B* **2003**, *67*, 035401.
[197] J.-T. Lü, R. B. Christensen, G. Foti, T. Frederiksen, T. Gunst, M. Brandbyge, *Phys. Rev. B* **2014**, *89*, 081405.

[198] M. Paulsson, T. Frederiksen, M. Brandbyge, *Nano Lett.* **2006**, *6*, 258.
[199] S. J. Altenburg, R. Berndt, *New J. Phys.* **2014**, *16*, 053036.
[200] S. Zhu, Y. Huang, N. N. Klimov, D. B. Newell, N. B. Zhitenev, J. A. Stroscio, S. D. Solares, T. Li, *Phys. Rev. B* **2014**, *90*, 075426.
[201] M. L. N. Palsgaard, N. P. Andersen, M. Brandbyge, *Phys. Rev. B* **2015**, *91*, 121403.
[202] S. J. Altenburg, J. Kröger, T. O. Wehling, B. Sachs, A. I. Lichtenstein, R. Berndt, *Phys. Rev. Lett.* **2012**, *108*, 206805.
[203] P. Roos, E. Bertel, K. Rendulic, *Chem. Phys. Lett.* **1995**, *232*, 537.
[204] N. Memmel, E. Bertel, *Phys. Rev. Lett.* **1995**, *75*, 485.
[205] J. Wiebe, F. Meier, K. Hashimoto, G. Bihlmayer, S. Blügel, P. Ferriani, S. Heinze, R. Wiesendanger, *Phys. Rev. B* **2005**, *72*, 193406.
[206] L. Ramoino, M. von Arx, S. Schintke, A. Baratoff, H.-J. Güntherodt, T. Jung, *Chem. Phys. Lett.* **2006**, *417*, 22.
[207] C. Bombis, N. Kalashnyk, W. Xu, E. Lægsgaard, F. Besenbacher, T. R. Linderoth, *Small* **2009**, *5*, 2177.
[208] J. Repp, G. Meyer, S. M. Stojković, A. Gourdon, C. Joachim, *Phys. Rev. Lett.* **2005**, *94*, 026803.
[209] Y. Wang, J. Kröger, R. Berndt, H. Tang, *J. Am. Chem. Soc.* **2010**, *132*, 12546.
[210] Y. Wang, K. Wu, J. Kröger, R. Berndt, *AIP Adv.* **2012**, *2*, 041402.
[211] E. Tsiper, Z. Soos, W. Gao, A. Kahn, *Chem. Phys. Lett.* **2002**, *360*, 47.
[212] S. Berner, M. de Wild, L. Ramoino, S. Ivan, A. Baratoff, H.-J. Güntherodt, H. Suzuki, D. Schlettwein, T. A. Jung, *Phys. Rev. B* **2003**, *68*, 115410.
[213] T. Schwieger, H. Peisert, M. Knupfer, *Chem. Phys. Lett.* **2004**, *384*, 197.
[214] M. Gorgoi, D. Zahn, *Org. Electron.* **2005**, *6*, 168.
[215] H. Peisert, A. Petershans, T. Chassé, *J. Phys. Chem. C* **2008**, *112*, 5703.
[216] Y. Wang, R. Yamachika, A. Wachowiak, M. Grobis, M. F. Crommie, *Nat. Mater.* **2008**, *7*, 194.
[217] M. Häming, C. Scheuermann, A. Schöll, F. Reinert, E. Umbach, *J. Electron Spectrosc. Relat. Phenom.* **2009**, *174*, 59.
[218] Y. Wang, J. Kröger, R. Berndt, W. Hofer, *Angew. Chem., Int. Ed.* **2009**, *48*, 1261.
[219] T. G. Gopakumar, T. Brumme, J. Kröger, C. Toher, G. Cuniberti, R. Berndt, *J. Phys. Chem. C* **2011**, *115*, 12173.
[220] X. H. Qiu, G. V. Nazin, W. Ho, *Phys. Rev. Lett.* **2004**, *92*, 206102.
[221] S. W. Wu, G. V. Nazin, X. Chen, X. H. Qiu, W. Ho, *Phys. Rev. Lett.* **2004**, *93*, 236802.
[222] F. Matino, G. Schull, F. Köhler, S. Gabutti, M. Mayor, R. Berndt, *Proc. Natl. Acad. Sci. USA* **2011**, *108*, 961.
[223] F. Schwarz, Y. F. Wang, W. A. Hofer, R. Berndt, E. Runge, J. Kröger, *J. Phys. Chem. C* **2015**, *119*, 15716.
[224] A. Mehler, N. Néel, M.-L. Bocquet, J. Kröger, *J. Phys.: Condens. Matter* **2018**, *31*, 065001.
[225] X. H. Qiu, G. V. Nazin, W. Ho, *Science* **2003**, *299*, 542.
[226] F. Rossel, M. Pivetta, W.-D. Schneider, *Surf. Sci. Rep.* **2010**, *65*, 129.
[227] K. Kuhnke, C. Große, P. Merino, K. Kern, *Chem. Rev.* **2017**, *117*, 5174.
[228] S. W. Wu, G. V. Nazin, W. Ho, *Phys. Rev. B* **2008**, *77*, 205430.
[229] C. Chen, P. Chu, C. A. Bobisch, D. L. Mills, W. Ho, *Phys. Rev. Lett.* **2010**, *105*, 217402.
[230] M. C. Chong, L. Sosa-Vargas, H. Bulou, A. Boeglin, F. Scheurer, F. Mathevet, G. Schull, *Nano Lett.* **2016**, *16*, 6480.
[231] Y. Zhang, Y. Luo, Y. Zhang, Y.-J. Yu, Y.-M. Kuang, L. Zhang, Q.-S. Meng, Y. Luo, J.-L. Yang, Z.-C. Dong, J. G. Hou, *Nature* **2016**, *531*, 623.
[232] H. Imada, K. Miwa, M. Imai-Imada, S. Kawahara, K. Kimura, Y. Kim, *Nature* **2016**, *538*, 364.
[233] B. Doppagne, M. C. Chong, E. Lorchat, S. Berciaud, M. Romeo, H. Bulou, A. Boeglin, F. Scheurer, G. Schull, *Phys. Rev. Lett.* **2017**, *118*, 127401.
[234] Y. Zhang, Q.-S. Meng, L. Zhang, Y. Luo, Y.-J. Yu, B. Yang, Y. Zhang, R. Esteban, J. Aizpurua, Y. Luo, J.-L. Yang, Z.-C. Dong, J. G. Hou, *Nat. Commun.* **2017**, *8*, 15225.
[235] H. Imada, K. Miwa, M. Imai-Imada, S. Kawahara, K. Kimura, Y. Kim, *Phys. Rev. Lett.* **2017**, *119*, 013901.
[236] L. Zhang, Y.-J. Yu, L.-G. Chen, Y. Luo, B. Yang, F.-F. Kong, G. Chen, Y. Zhang, Q. Zhang, Y. Luo, J.-L. Yang, Z.-C. Dong, J. Hou, *Nat. Commun.* **2017**, *8*, 580.
[237] J. Kröger, B. Doppagne, F. Scheurer, G. Schull, *Nano Lett.* **2018**, *18*, 3407.
[238] G. Profeta, M. Calandra, F. Mauri, *Nat. Phys.* **2012**, *8*, 131.
[239] S. Simon, E. Voloshina, J. Tesch, F. Förschner, V. Enenkel, C. Herbig, T. Knispel, A. Tries, J. Kröger, Y. Dedkov, M. Fonin, *Small* **2018**, *14*, 1703701.
[240] G. Li, A. Luican, J. M. B. Lopes dos Santos, A. H. Castro Neto, A. Reina, J. Kong, E. Y. Andrei, *Nat. Phys.* **2010**, *6*, 109.